Title

Nucleation seed size determines amyloid clearance and establishes a barrier to prion appearance in yeast

Journal

Nature Structural & Molecular Biology, 27(6)

ISSN

1545-9993

Authors

Villali, Janice
Dark, Jason
Brechtel, Teal M
et al.

Publication Date

2020-06-01

DOI

10.1038/s41594-020-0416-6

Peer reviewed

HHS Public Access

Author manuscript

Nat Struct Mol Biol. Author manuscript; available in PMC 2020 November 04.

Published in final edited form as:

Nat Struct Mol Biol. 2020 June ; 27(6): 540–549. doi:10.1038/s41594-020-0416-6.

Nucleation seed size determines amyloid clearance and establishes a barrier to prion appearance in yeast

Janice Villali[1,‡,†], **Jason Dark**[2,‡], **Teal M. Brechtel**[3], **Fen Pei**[3,^], **Suzanne S. Sindi**[2,*], **Tricia R. Serio**[4,*]

[1]Department of Molecular Biology, Cell Biology and Biochemistry, Brown University, Providence, RI

[2]Department of Applied Mathematics, The University of California, Merced, Merced, CA

[3]Department of Molecular and Cellular Biology, The University of Arizona, Tucson, AZ

[4]Department of Biochemistry and Molecular Biology, The University of Massachusetts Amherst, Amherst, MA

Abstract

Amyloid appearance is a rare event that is promoted in the presence of other aggregated proteins. These aggregates were thought to act by templating the formation of an assembly-competent nucleation seed, but we find an unanticipated role for them in enhancing the persistence of amyloid after it arises. Specifically, *Saccharoymyces cerevisiae* Rnq1 amyloid reduces chaperone-mediated disassembly of Sup35 amyloid, promoting its persistence in yeast. Mathematical modeling and corresponding *in vivo* experiments link amyloid persistence to the conformationally defined size of the Sup35 nucleation seed and suggest that amyloid is actively cleared by disassembly below this threshold to suppress appearance of the [*PSI*$^+$] prion *in vivo*. Remarkably, this framework resolves multiple known inconsistencies in the appearance and curing of yeast prions. Thus, our observations establish the size of the nucleation seed as a previously unappreciated characteristic of prion variants that is key to understanding transitions between prion states.

The appearance of amyloid *in vivo* is associated with physiological changes ranging from the emergence of incurable neurodegenerative disease to the establishment of alternative and heritable gene expression states.[1] While the conformational basis of these phenomena are intriguing, the true significance of this process is its capacity to create dynamic phenotypes,

*Correspondence to: ssindi@ucmerced.edu; tserio@umass.edu.
†Present addresses: KSQ Therapeutics, Cambridge MA 02139
^BioLegend, San Diego, CA 92121
‡These authors contributed equally to this work.

Author Contributions

J.V. and J.D. conceptualized and designed the work, acquired, analyzed and interpreted data, and drafted and revised the manuscript. T.M.B. and F.P. acquired, analyzed and interpreted data and revised the manuscript. S.S.S. and T.R.S. conceptualized and designed the work, analyzed and interpreted data, and drafted and revised the manuscript.

Competing Interests

The authors declare no competing interests.

which can arise and be lost within the lifetime of an organism.[1] Despite the impact of these transitions, our understanding of the biochemical processes limiting amyloid appearance and clearance *in vivo*, both extremely rare events, lags considerably far behind.[2,3]

At the biochemical level, amyloid formation is a multi-step process in which non-native conformers of proteins arise and assemble into kinetically stable, linear aggregates with cross-β structure.[2] Once these aggregates appear, they act as templates for further assembly, and such templating capacity is amplified by growth to increase the surface area for lateral assembly and/or by fragmentation to create new ends for extension.[4–7] The barrier to amyloid formation *in vitro* is the assembly of a nucleus of minimum defined size, which represents a local turning point demarcating the transition from thermodynamically unfavored to favored associations.[8] The concentration dependence of the nucleation process is thought to be the major factor limiting the spontaneous appearance of amyloid *in vivo*.[8,9] Once formed, the nucleus rapidly incorporates additional monomers, leading to the formation of a thermodynamically stable aggregate of minimum size n_s, previously termed the minimum nucleation seed,[10] and hereafter referred to as “seed” (Fig. 1a). Aggregates below the size of this seed spontaneously disassemble, returning protein to the soluble state (Fig. 1a, orange species).

Despite this barrier, the frequency of amyloid appearance from yeast to man is elevated during aging and stress, likely due in part to the presence of other misfolded and aggregated proteins or amyloids.[11–16] A well-characterized and experimentally tractable example of this effect, known as proteostasis collapse, is the appearance of the yeast prion [*PSI*$^+$], which is determined by the amyloid form of the Sup35 protein.[17–25] [*PSI*$^+$] can arise spontaneously or following transient overexpression of Sup35 but only in yeast strains propagating the [*PIN*$^+$] (inducible to [*PSI*$^+$]) prion, which is most often determined by the amyloid form of the Rnq1 protein.[13,14,26] The favored model suggests that Rnq1 amyloid acts as a heterologous template for the direct assembly of Sup35 seeds *in vivo*. However, key predictions of this model, including a link between the frequency of [*PSI*$^+$] appearance and either the accumulation of Rnq1 amyloid or its association with Sup35, have not been demonstrated.[3] More generally, while direct interactions between amyloidogenic proteins are thought to occur,[27] the specificity of amyloid co-polymerization and cross-seeding is seemingly incompatible with the broad range of proteins that intersect during proteostasis collapse. Thus, this promotion of amyloid formation could occur through other currently unexplored pathways.[13–15,28–30]

Indeed, quantitative analyses of amyloid dynamics *in vivo* for both yeast and mammalian prions suggest several additional points of potential regulation. Specifically, the phenotypic appearance of a stable amyloid state requires that, once a seed is formed, it persists, amplifies and faithfully transmits to reach its steady-state accumulation in an organism.[4,31,32] Disruption of any of these steps, including seed formation itself, results in the same observable outcome: the failure to acquire the amyloid-associated phenotype. Consistent with this idea, the frequency and variant of prion appearing in yeast and mammals following introduction or spontaneous formation of amyloid can be modified by inoculation routes or timing and selection conditions, indicating regulation after seed formation.[16,33–36] These observations raise the possibility that misfolded and aggregated proteins or amyloids can act

at regulatory steps subsequent to seed formation to promote amyloid appearance by other proteins, an idea that has been largely untested.[3]

Here, we demonstrate that the [*PIN*$^+$] prion can act after seed formation to promote [*PSI*$^+$] appearance by titrating the binding of the molecular disaggregase Hsp104 to Sup35 amyloid. Unexpectedly, we link the alternative outcomes of this interaction – clearance of amyloid or transition to a stable amyloid state – to a previously unappreciated characteristic of prion conformational variants: the size of the seed. We demonstrate that differences in seed size are crucial to mechanistically capture prion appearance and curing and permit the resolution of previously confounding observations for prion transitions in yeast.

Results

[PIN$^+$] promotes [PSI$^+$] appearance subsequent to Sup35 seed formation

To explore the impact of [*PIN*$^+$] on events subsequent to seed formation, we assessed [*PSI*$^+$] appearance following the transfection of *in vitro* assembled amyloid fibers of the Sup35 prion-determining domain (NM; aa 1–254)[19] into yeast. This approach bypasses the requirement for *de novo* seed formation and does not require [*PIN*$^+$].[37,38] Previous studies suggested that delivery of a single amyloid fiber was sufficient to convert yeast from the [*psi*$^-$] (non-prion) to the [*PSI*$^+$] state.[31] We repeated this analysis by transfecting non-prion yeast ([*psi*$^-$][*pin*$^-$]) or those with the [*PIN*$^+$] prion alone with amyloid fibers assembled from two different conformers of Sup35, Sc4 and Sc37 (*n.b.* Sc4 is fragmented at a higher rate than Sc37).[37] We then compared the fit of the concentration-dependence of [*PSI*$^+$] appearance to models using one to three fibers (see Supplementary Note 1) as has been previously done.[30] Although the [*PIN*$^+$] and [*pin*$^-$] conditions were best fit to the one fiber model for both Sc4 and Sc37 amyloid (Extended Data Fig. 1), these fits required a distribution of transfection efficiencies with different means (λ) for [*PIN*$^+$] and [*pin*$^-$] strains (Supplementary Table 1). As transfection efficiencies are not predicted to vary with prion state, this distinction reveals the contribution of another, currently unknown factor beyond the uptake of a single fiber to the establishment of a stable prion state.

Intriguingly, [*PIN*$^+$] had minimal impact on the concentration-dependent appearance of [*PSI*$^+$] using Sc4 amyloid (Fig. 1b) but promoted [*PSI*$^+$] appearance at lower concentrations of Sc37 amyloid (Fig. 1c). The positive impact of [*PIN*$^+$] following delivery of pre-formed Sc37 amyloid indicates a role for this factor in [*PSI*$^+$] appearance at a step subsequent to seed formation.

[PIN$^+$] titrates Hsp104 activity on Sup35 amyloid to promote [PSI$^+$] appearance

Our previous studies revealed that existing Sup35 amyloid is cleared from cells with an elevated rate of fragmentation catalyzed by the molecular chaperone Hsp104 and its co-chaperones Hsp70 (Ssa1/2) and Hsp40 (Sis1).[20,39–45] We reasoned that during seed formation, chaperone levels would far exceed those of amyloid, potentially creating a situation in which a nascent seed is cleared before growth and fragmentation amplifies this form to establish a stable prion state. To test this idea, we genetically reduced the level of Hsp104, the final actor in the chaperone cascade leading to amyloid fragmentation, by

creating a heterozygous disruption and compared the appearance of [*PSI*$^{+}$] following transfection of Sc37 amyloid fibers into *HSP104/HSP104* or *HSP104/Δ* diploid yeast strains in the presence or absence of [*PIN*$^{+}$]. In the [*pin*$^{-}$] strain, heterozygous disruption of *HSP104* promoted [*PSI*$^{+}$] appearance at slightly lower concentrations of Sc37 amyloid relative to wildtype (Fig. 1d), mirroring the effect of [*PIN*$^{+}$] albeit at a slightly lower magnitude (Fig. 1c). In the [*PIN*$^{+}$] strain, this effect was reversed: [*PSI*$^{+}$] appearance occurred at slightly higher concentrations of Sc37 amyloid relative to wildtype in a strain with a heterozygous disruption of *HSP104* (Fig. 1e).

What is the basis of this effect? Rnq1 amyloid is a substrate of Hsp104.[26,46] If Rnq1 amyloid competes with nascent Sup35 seeds for access to Hsp104, the rate of disassembly of Sup35 seeds through fragmentation would be reduced, perhaps allowing it to persist and be amplified. When this reduction is mild (i.e. the presence of [*PIN*$^{+}$] alone), [*PSI*$^{+}$] appearance is promoted because the balance is optimized: nascent Sup35 seeds persist and are amplified at a rate that sustains amyloid in the population of dividing cells. However, when this reduction is more pronounced, [*PSI*$^{+}$] appearance is slightly reduced (i.e. heterozygous disruption of *HSP104* alone) or inhibited (i.e. the combination of heterozygous disruption of *HSP104* and [*PIN*$^{+}$]) relative to the presence of [*PIN*$^{+}$] alone, presumably because the rate of amplification of amyloid aggregates by fragmentation is decreased to a level insufficient to sustain the prion state in a dividing population of cells.

If this hypothesis is accurate, [*PIN*$^{+}$] should reduce the fragmentation of existing Sup35 amyloid as well. We tested this idea using yeast strains with naturally occurring [*PSI*$^{+}$] variants known as [*PSI*$^{+}$]^{Strong} (~[*PSI*$^{+}$]^{Sc4}) and [*PSI*$^{+}$]^{Weak} (~[*PSI*$^{+}$]^{Sc37})[31,47]. Heterozygous disruption of *HSP104* in a [*PSI*$^{+}$]^{Strong} strain (Extended Data Fig. 1a) induced a slight increase in the steady-state size of Sup35 amyloid by semi-denaturing detergent agarose gel electrophoresis (SDD-AGE) and immunoblotting (Fig. 1f) but did not alter the fraction of aggregated Sup35 (Fig. 1g) or total Sup35 levels (Extended Data Fig. 1b), suggesting a minor reduction in fragmentation efficiency.[32] Notably, homozygous disruption of *RNQ1* (Extended Data Fig. 1c), which eliminates [*PIN*$^{+}$],[13,14] did not alter this effect (Fig. 1f), consistent with the insensitivity of [*PSI*$^{+}$] appearance to the presence of [*PIN*$^{+}$] upon transfection of Sc4 amyloid (Fig. 1b). In contrast, heterozygous disruption of *HSP104* (Extended Data Fig. 1a) severely inhibited the propagation of [*PSI*$^{+}$]^{Weak} in the presence of [*PIN*$^{+}$], strongly reducing the accumulation of aggregates and increasing the fraction of soluble Sup35 (Fig. 1g, h) without altering total Sup35 levels (Extended Data Fig. 1b). Strikingly, elimination of [*PIN*$^{+}$] by homozygous disruption of *RNQ1* (Extended Data Fig. 1c) reversed the impact of heterozygous disruption of *HSP104* on [*PSI*$^{+}$]^{Weak} propagation by restoring the accumulation of Sup35 aggregates (Fig. 1h) and partially reducing the fraction of soluble Sup35 (Fig. 1g). This effect can be explained by an increase in fragmentation rate, as Sup35 aggregates shifted to a faster migrating species in a strain with a wildtype complement of *HSP104* and a homozygous disruption of *RNQ1* (Fig. 1h). These observations again paralleled the effects of similar manipulations on [*PSI*$^{+}$] appearance upon transfection of Sc37 amyloid (Fig. 1d, e). Thus, the fragmentation defect induced by heterozygous disruption of *HSP104* is exacerbated by [*PIN*$^{+}$], consistent with the idea that Rnq1 and Sup35 amyloid compete for access to Hsp104. Notably, the presence of [*PSI*$^{+}$] did not alter the accumulation or size of Rnq1 amyloid as previously reported[48] even in a strain

with a heterozygous disruption of *HSP104* (Fig. 2a), indicating that Hsp104 is limiting for [*PSI*$^+$] but not [*PIN*$^+$] fragmentation when both prions are present.

To determine if changes in Hsp104 levels could similarly modulate [*PSI*$^+$] appearance under conditions requiring formation of Sup35 amyloid seeds *de novo*, we transiently overexpressed NM from a copper-inducible promoter in wildtype or *HSP104/Δ* [*psi*$^-$] [*PIN*$^+$] strains (Extended Data Fig. 2a). As determined by a fluctuation test,[49] [*PSI*$^+$] appeared at a rate of 1.8×10^{-7} cells per generation in a wildtype strain, representing an approximately 3-fold increase over the uninduced control (Fig. 2b). Heterozygous disruption of *HSP104* significantly increases this rate, by ~ 2.3 fold (Fig. 2b) without altering total Sup35 levels (Extended Data Fig. 2b). This enhancement is likely an underestimate, as the heterozygous disruption of *HSP104* promoted a low rate of [*PSI*$^+$] loss (Extended Data Fig. 2c). Importantly, heterozygous disruption of *HSP104* does not impact [*PIN*$^+$] propagation directly: the size of SDS-resistant (Fig. 2a) and native (Fig. 2c) Rnq1 aggregates, the accumulation of total and soluble Rnq1 protein (Fig. 2d), and the number of heritable Rnq1 particles (Fig. 2e), were all similar in wildtype and *HSP104/Δ* strains. Thus, wildtype Hsp104 levels restrict the appearance of [*PSI*$^+$] not only following transfection of amyloid (Fig. 1d) but also during its *de novo* formation.

If fragmentation does reduce [*PSI*$^+$] appearance through disassembly of newly formed Sup35 amyloid, this effect should be exacerbated in the presence of excess Hsp104. Previous studies have reported that co-overexpression of Hsp104 and NM-GFP or full-length Sup35 reduced [*PSI*$^+$] appearance.[50–52] To quantitatively examine the impact of Hsp104 overexpression on *de novo* [*PSI*$^+$] appearance in a more controlled setting, we overexpressed NM in a [*PIN*$^+$] strain expressing an extra copy of *HSP104* (Extended Data Fig. 2a), which did not alter the expression of full-length Sup35 (Extended Data Fig. 2b), and quantified the rate of [*PSI*$^+$] appearance using a fluctuation test. Indeed, the rate of [*PSI*$^+$] appearance was reduced by ~2.7-fold in the presence of excess Hsp104 relative to a wildtype strain (Fig. 2b). This effect could not be fully explained by the reduced stability of existing [*PSI*$^+$] under the same conditions (~1.2–1.9-fold loss, Extended Data Fig. 2c), suggesting that excess Hsp104 also reduces prion appearance as predicted by our model.

Taken together, our observations indicate that Hsp104 levels impose a biologically relevant and [*PIN*$^+$]-dependent limit on the appearance of a stable [*PSI*$^+$] state after the formation of a Sup35 seed. If [*PIN*$^+$] indeed acts by competing with [*PSI*$^+$] for Hsp104, we would expect Hsp104 binding to Sup35 amyloid to increase upon elimination of [*PIN*$^+$]. To test this idea, we expressed HA-tagged NM in [*PIN*$^+$] and [*pin*$^-$] strains propagating either the [*PSI*$^+$]^{Strong} or [*PSI*$^+$]^{Weak} prion variants, quantitatively immunocaptured the tagged protein and the co-aggregated full-length Sup35,[53] and assessed Hsp104 binding by SDS-PAGE and immunoblotting. While previous qualitative observations did not capture [*PIN*$^+$]-dependent differences in chaperone binding to Sup35,[54] our optimized conditions revealed that Hsp104 binding to Sup35 aggregates in a [*PSI*$^+$]^{Strong} strain increased by ~12% when [*PIN*$^+$] was eliminated (Fig. 2f, Extended Data Fig. 2d), providing direct evidence of competition. Remarkably, the loss of [*PIN*$^+$] had an even greater effect on Hsp104 binding to Sup35 aggregates in a [*PSI*$^+$]^{Weak} strain, increasing its association by ~23% (Fig. 2f, Extended Data Fig. 2d). This observation suggests that Sup35 aggregates in the [*PSI*$^+$]^{Weak} conformation

compete less efficiently with Rnq1 aggregates in the [*PIN*$^+$] strain for Hsp104 binding than Sup35 aggregates in the [*PSI*$^+$]^{Strong} conformation. This difference provides a direct explanation for the enhanced sensitivity of this variant to the presence of [*PIN*$^+$] in fiber transfection experiments (Fig. 1b, c). Together, these observations indicate that [*PIN*$^+$] promotes the appearance of a stable [*PSI*$^+$] state by reducing Hsp104 binding to and chaperone-mediated disassembly of Sup35 amyloid.

Prion variant-dependent differences in seed size predict sensitivity to disassembly

Our observations on [*PSI*$^+$] appearance following transfection of Sup35 amyloid into yeast (Fig. 1b–e) and our previous work studying [*PSI*$^+$] curing in response to transient heat shock[45] indicate that the [*PSI*$^+$]^{Weak}/[*PSI*$^+$]^{Sc37} variant is more sensitive to clearance by chaperone-mediated fragmentation than the [*PSI*$^+$]^{Strong}/[*PSI*$^+$]^{Sc4} variant. This interpretation, however, is not consistent with the observation that the [*PSI*$^+$]^{Weak}/[*PSI*$^+$]^{Sc37} variant has a lower rate of fragmentation than the [*PSI*$^+$]^{Strong}/[*PSI*$^+$]^{Sc4} variant both *in vitro* and *in vivo*.[31,32,43] Our inability to reconcile these observations suggests that our understanding of the biochemical processes balancing amyloid assembly and clearance are incomplete.

To bridge this gap, we sought to determine a minimal model for the stable propagation of the [*PSI*$^+$] phenotype by considering both deterministic and stochastic mathematical models of Sup35 aggregate dynamics *in vivo* based on nucleated polymerization dynamics (Fig. 1a, Supplementary Note 1). Nucleated polymerization dynamics model Sup35 aggregates as linear and stable above a minimum size n_s (i.e. the seed); these complexes grow bi-directionally through the addition of monomers to their ends and can be fragmented at any monomer-monomer interface to create two aggregates that persist when their sizes are greater than or equal to n_s. To specifically capture the stochastic effects present when a cell contains small numbers of amyloid aggregates,[55] we developed a new stochastic persistence model, which considers the irreversible condition where a single aggregate is introduced into a cell and the probability that it successfully creates a second aggregate greater than or equal to size n_s before cell division. Aggregates below size n_s, spontaneously disassemble and thereby prohibit each cell from inheriting an aggregate, which is the minimum requirement for stable propagation of amyloid in a population of dividing cells.

We assessed persistence of Sup35 amyloid in our stochastic model over a broad range of values for the conversion (β) and fragmentation (γ) rates at a constant seed size (n_s) of five. In contrast to previous studies,[31,32] this approach allows us to rigorously assess the probability of loss of a single Sup35 aggregate as a function of fragmentation rate for the first time (Fig. 3a). Importantly, our stochastic persistence model correctly captured the factors known to promote [*PSI*$^+$] appearance, including an increase in Sup35 expression (Extended Data Fig. 3a) and an increase in the number of Sup35 aggregates (Extended Data Fig. 3b). Moreover, unlike previous models[31,32] but consistent with our observations above, the stochastic persistence model captured a decrease in the probability of [*PSI*$^+$] persisting at both high and low fragmentation rates (Fig. 3a, b).

With this broad agreement of the model to experiments, we next sought to determine the positions of the [*PSI*$^+$]^{Strong}/[*PSI*$^+$]^{Sc4} and [*PSI*$^+$]^{Weak}/[*PSI*$^+$]^{Sc37} variants in parameter

space. As was done previously, we determined conversion and fragmentation rates for each variant by requiring that the steady-state values obtained from a deterministic model based on nucleated polymerization dynamics agree with the average aggregate size and soluble fraction of Sup35 (Supplementary Table 2, Extended Data Fig. 3c).[31,32] These values captured both the decrease in aggregate size upon inhibition of Sup35 synthesis, which limits conversion and allows fragmentation to dominate the aggregate dynamics (Extended Data Fig. 4a, b),[32] and an increase in aggregate size upon inhibition of fragmentation, which allows conversion to dominate the aggregate dynamics (Extended Data Fig. 4c, d).[32] Based on these analyses, $[PSI^{+}]^{Strong}/[PSI^{+}]^{Sc4}$ existed at a higher fragmentation rate (γ) than $[PSI^{+}]^{Weak}/[PSI^{+}]^{Sc37}$ within the stable amyloid zone (Fig. 3b, square vs. triangle, respectively). Surprisingly, these parameter values place $[PSI^{+}]^{Strong}/[PSI^{+}]^{Sc4}$ closer to the boundary between stability and instability at high fragmentation rates than $[PSI^{+}]^{Weak}/[PSI^{+}]^{Sc37}$ (Fig. 3b), suggesting an increased sensitivity of $[PSI^{+}]^{Strong}/[PSI^{+}]^{Sc4}$ to clearance. This mathematical prediction is incompatible with *in vivo* observations of both prion appearance (Fig. 1b, c) and heat shock-mediated prion curing,[45] which both promote clearance of $[PSI^{+}]^{Weak}/[PSI^{+}]^{Sc37}$ over $[PSI^{+}]^{Strong}/[PSI^{+}]^{Sc4}$ at elevated fragmentation rates. Thus, the biochemical rates of conversion and fragmentation, which have been used to define prion conformational variants at steady-state,[31,32] cannot capture their differential behavior during prion appearance and loss, events that are key to their epigenetic character and impact.

In classic schemes of nucleated growth such as sickle hemoglobin polymerization, nucleus size, and thereby seed size, is a continuous value that depends on both the solution conditions and the free monomer concentration.[56] To our knowledge, amyloid seed size has not been proposed to vary *in vivo*, as the same protein is expressed to the same level in the same cellular context. Nonetheless, our mathematical modeling indicated that it could be the missing factor needed to capture the enhanced sensitivity of $[PSI^{+}]^{Weak}/[PSI^{+}]^{Sc37}$ to increased fragmentation. Amyloid clearance by fragmentation is predicted to occur through the progressive decrease in aggregate size until n_s is reached; at this point, further fragmentation will reduce the aggregate below the minimal stable size and lead to rapid disassembly (Fig. 1a). Amyloid aggregates with a larger n_s have an increased window of sensitivity to clearance by this mechanism because they must convert a larger number of monomers to reach a size of $2n_s$ (Fig. 3c, upper boundary), which is the minimum size that could produce two stable aggregates following a single fragmentation event. Consistent with this idea, progressive increases in seed size are predicted to have little effect on amyloid persistence at low rates of fragmentation but their greatest and size-dependent impact at high rates of fragmentation (Fig. 3a, white dashed line, 3d). Thus, an amyloid aggregate with a smaller n_s is more robust to chaperone-mediated disassembly and clearance.

Based on this logic, the increased sensitivity of $[PSI^{+}]^{Weak}/[PSI^{+}]^{Sc37}$ to fragmentation-mediated clearance could be explained if it has a larger n_s than $[PSI^{+}]^{Strong}/[PSI^{+}]^{Sc4}$. Indeed, increasing n_s from five to fifteen for $[PSI^{+}]^{Weak}/[PSI^{+}]^{Sc37}$ and adjusting the conversion (β) and fragmentation (γ) rates to capture the appropriate steady-state aggregate size and soluble fraction (Supplementary Table 2, Extended Data Fig. 3c) shifted this variant to a precipice in the stochastic persistence model, where a slight increase or decrease in fragmentation rate would lead to $[PSI^{+}]$ loss (Fig. 3b, circle on right). This situation contrasts with that of the $[PSI^{+}]^{Strong}/[PSI^{+}]^{Sc4}$ variant, which is predicted to remain stable

to similar perturbations (Fig. 3b, square on left). These mathematical predictions capture the relative sensitivity of the variants to the same manipulations *in vivo*.[45,57] Notably, [*PSI*$^{+}$]^{Weak}/[*PSI*$^{+}$]^{Sc37} fell far from the peak probability of amplification in the stochastic persistence model when its seed size is five (Fig. 3e, circle), but both variants fell close to this peak at seed sizes that capture their relative sensitivities to fragmentation (i.e. five for [*PSI*$^{+}$]^{Strong}/[*PSI*$^{+}$]^{Sc4} and fifteen for [*PSI*$^{+}$]^{Weak}/[*PSI*$^{+}$]^{Sc37}, Fig. 3e, squares). Moreover, the peak occurred at a lower fragmentation rate for the [*PSI*$^{+}$]^{Weak}/[*PSI*$^{+}$]^{Sc37} than for [*PSI*$^{+}$]^{Strong}/[*PSI*$^{+}$]^{Sc4} (Fig. 3e), as observed in our amyloid transfection experiments (Fig. 1b, c). Thus, the parameters defining the two conformational variants (β, γ, n_s) indicate that these states are optimal for [*PSI*$^{+}$] appearance.

While the range of seed sizes used in our modeling are consistent with the minimum sizes previously reported for [*PSI*$^{+}$]^{Strong} and [*PSI*$^{+}$]^{Weak} amyloid distributions,[58] we cannot determine the absolute seed size more directly because the *in vitro* kinetics of Sup35 amyloid assembly are dominated by secondary nucleation events.[6] To experimentally interrogate these mathematical predictions, we, therefore, determined relative seed sizes for the [*PSI*$^{+}$]^{Strong} and [*PSI*$^{+}$]^{Weak} variants *in vivo*. Our deterministic system reveals that upon inhibition of Sup35 synthesis, the aggregate size distribution shifted to smaller sizes but does not breach n_s, because aggregates below this size are disassembled (Extended Data Fig. 4a, b). This shift occurred over an extended period for [*PSI*$^{+}$]^{Weak} with a seed size of five (Extended Data Fig. 4e, f, g); however, the shift is predicted to rapidly reach its full extent for [*PSI*$^{+}$]^{Strong} with seed size of five (Extended Data Fig. 4a) and [*PSI*$^{+}$]^{Weak} with a seed size of fifteen (Extended Data Fig. 4b, h), parameters that capture the relative sensitivities of the variants to fragmentation (Fig. 3b). Thus, this approach can be used to report on relative seed size *in vivo*.

We replicated this process *in vivo* by treating [*PSI*$^{+}$]^{Strong} and [*PSI*$^{+}$]^{Weak} strains with cycloheximide and monitoring the lower boundary of the aggregate size distribution. Sup35 aggregates in the [*PSI*$^{+}$]^{Strong} strain shifted to faster migrating species than those in the [*PSI*$^{+}$]^{Weak} strain (Fig. 4a). This observation indicates that [*PSI*$^{+}$]^{Strong} has a smaller n_s than [*PSI*$^{+}$]^{Weak}, as predicted by our stochastic persistence model, and suggests that seed size is the missing parameter capturing the differential behavior of Sup35 conformational variants during prion appearance and loss.

Variations in seed size resolve conundrums during prion transitions in yeast

To determine if n_s differences can explain other confounding fragmentation-mediated [*PSI*$^{+}$] transitions, we assessed the size of the Sup35 amyloid seed for three situations. First, we compared the seed sizes of amyloid composed of wildtype Sup35 with that composed of the R2E1 sequence variant of Sup35. R2E1 promotes a high frequency of spontaneous [*PSI*$^{+}$] appearance[59] (Fig. 4b) but has a high rate of fragmentation,[60] which are incompatible characteristics if chaperone-mediated disassembly clears nascent Sup35 seeds. Our model predicts that R2E1 amyloid persistence at this higher rate of fragmentation can only occur if the R2E1 seed is smaller than that of wildtype Sup35 (Fig. 3d). Indeed, R2E1 aggregates shifted to a faster migrating species than that of wildtype Sup35 (Fig. 4c), indicating that the mutant has a smaller n_s.

Second, we compared the seed sizes of the [*PSI*$^{+}$]^{Weak} and [*PSI*$^{+}$]^{Sc37} variants. These variants have similar *in vivo* phenotypes and similar kinetic stabilities, suggesting they have similar rates of fragmentation *in vivo*.[43] Nonetheless, [*PSI*$^{+}$]^{Sc37} is lost more readily in the presence of the G58D mutant of Sup35,[43] which promotes fragmentation-mediated amyloid clearance.[44] Our model predicts that the increased sensitivity of [*PSI*$^{+}$]^{Sc37} to G58D expression can only be explained by a larger seed size (Fig. 3d). Indeed, Sup35 amyloid from the [*PSI*$^{+}$]^{Weak} strain shifted to a faster migrating species than that from the [*PSI*$^{+}$]^{Sc37} strain, indicating the latter has a larger n_s (Fig. 4d).

Third, we considered the conundrum revealed by comparing prion loss in response to G58D expression and heat shock. Both conditions promote fragmentation-mediated prion clearance; however, G58D expression preferentially cures [*PSI*$^{+}$]^{Strong}, and heat shock preferentially cures [*PSI*$^{+}$]^{Weak}.[44,45] Because our model predicts that sensitivity to enhanced fragmentation is associated with a larger seed (Fig. 3d), we predict that the incorporation of G58D into [*PSI*$^{+}$]^{Strong} amyloid composed of wildtype Sup35 increases its seed size. Indeed, Sup35 amyloid shifted to a faster migrating species than that of Sup35:G58D amyloid (Fig. 4e), indicating that the mixed amyloid has a larger n_s. Thus, seed size is a crucial factor impacting both prion appearance and clearance, and this commonality further suggests these two events are interrelated and opposing.

Discussion

Our studies indicate that establishment of a stable amyloid state requires both seed formation and persistence *in vivo* (Fig. 5). The size of an amyloid nucleus and thereby seed has long been appreciated as a significant barrier to amyloid formation because the rate of its assembly varies with the concentration of monomer raised to the power of $n_0 - 1$.[61] Given this relationship, the bypass of seed formation through heterologous templating has become the favored model to explain the promotion of amyloid formation by other aggregates. While our studies do not rule out heterologous templating for [*PIN*$^{+}$], significant gaps in experimental support for this model remain.[3] Independent of this open question, our findings reveal an unrelated role for [*PIN*$^{+}$] after seed formation to promote amplification rather than clearance of nascent Sup35 amyloid by titrating the activity of the molecular chaperone Hsp104 through direct competition for its binding.

Beyond [*PIN*$^{+}$], other aggregation-prone proteins have been proposed to promote [*PSI*$^{+}$] appearance upon their overexpression by titrating the chaperone machinery.[62,63] The evidence in support of such a model is most robust for overexpressed Pin4c, which co-localizes with Hsp104 and Sis1 in cytoplasmic foci, induces an increase in Sup35 aggregate size, and promotes loss of [*PSI*$^{+}$] that can be reduced by overexpression of Hsp104 or Sis1.[62] However, [*PIN*$^{+}$] was not previously demonstrated to alter the size of Sup35 aggregates at physiological levels of Rnq1,[48] as would be predicted if it acted to titrate chaperones.[3] Nonetheless, the ability of [*PIN*$^{+}$] to induce [*PSI*$^{+}$] loss under some conditions did demonstrate interference between the two prions.[64,65] Our studies reconcile these seemingly disparate observations by demonstrating dose dependency: the impact of [*PIN*$^{+}$] on [*PSI*$^{+}$] appearance and propagation becomes apparent when Hsp104 is limiting (Fig. 1 d, e, h), lending further support to a role for [*PIN*$^{+}$] in chaperone titration.

Our observations indicate that small changes in Hsp104 availability have a profound effect specifically on the persistence of nascent Sup35 amyloid, a feature captured by our mathematical model (Fig. 3e) and consistent with the magnitude of the reduction in Hsp104 binding to Sup35 amyloid in the presence of [*PIN*$^+$] (Fig. 2f). This exquisite sensitivity of nascent Sup35 amyloid to fragmentation rate also provides an alternative framework in which to view the interaction between prion variants. [*PIN*$^+$] variants were originally identified by their distinct efficiencies in promoting the frequency of [*PSI*$^+$] appearance *in vivo*[64] and were subsequently shown to differentially promote the appearance of [*PSI*$^+$] variants.[54,66] This variant specificity has been interpreted as support for the heterologous templating model of [*PSI*$^+$] appearance, perhaps through the stabilization of conformationally distinct seeds.[67] An alternative, but not mutually exclusive, interpretation is that [*PIN*$^+$] variants differ in their ability to titrate Hsp104 or other chaperones, leading to the persistence of conformationally distinct seeds. Consistent with this possibility, the variant of [*PSI*$^+$] induced *in vivo* is altered by changes in Hsp104 levels and activity or by the presence of different mutants of the heat-shock master regulator Hsf1,[51,52,68] and [*PIN*$^+$] variants are differentially sensitive to chaperone mutations.[69–73]

As revealed by our experimental observations and our development and validation of predictive mathematical models, the balance between the amplification and clearance of nascent seeds is a function not only of fragmentation activity, which is modulated by the presence of other aggregates, but also of seed size, which directly defines the outcome of a fragmentation event. The emergence of seed size as a previously unappreciated contributor to prion variant biology was unexpected. The steady-state behavior of prion variants can be captured completely with the nucleated polymerization model with two conformationally defined parameters: the rates of conversion (β) and fragmentation (γ).[31,32] Nonetheless, these aggregate dynamics are unable to account for prion transitions, revealing a mechanistic gap specific to the appearance and clearance of amyloid *in vivo*. By incorporating conformationally defined differences in seed size into the nucleated polymerization model, we capture for the first time the differential sensitivities of [*PSI*$^+$] variants to dominant-negative mutants and changes in proteostatic niche, suggesting that seed size is a fundamental mechanistic contributor to amyloid transitions in yeast.

Are our observations in yeast applicable to mammalian prion biology? Previous studies have demonstrated an empirical relationship between R_0, a factor related to incubation time for prion infectivity, and r, a factor related to the accumulation of protease-resistant PrP (PrP-res).[4,74] Our preliminary analyses of the same data suggest that the nucleated polymerization model is unable to mechanistically capture this relationship for prion variants using a constant seed size if their conformational stability is used as a proxy for their relative fragmentation rates.[75] This gap raises the possibility that variations in seed size could provide new mechanistic insight into prion transitions in mammals, as we have demonstrated for yeast. Consistent with this idea, a metazoan disaggregase machinery capable of resolving amyloid *in vivo* and *in vitro* has been identified, and strikingly, this resolution occurs through a shift in amyloid size to a minimum threshold as we have observed for Sup35.[76,77] These observations, along with the increase in amyloid appearance with the decline of the proteostasis network during aging,[11,12] suggest that an interacting network of similar parameters may limit amyloid appearance in higher eukaryotes. If that is the case,

therapeutics aimed at shifting amyloid variants to conformers with increased seed size, as we have demonstrated for incorporation of G58D into Sup35 amyloid, could emerge as effective complements to proteostasis modulators in the treatment of protein misfolding diseases.

Methods

S. cerevisiae Strains

All yeast strains used in this study are derivatives of 74D-694[20] and are listed in Supplementary Table 3. Disruptions of *RNQ1* were generated by transfection of PCR-generated cassettes using pFA6aKanMX4 or pFA6a-CaURA3MX4 as a template with the indicated primers (MSO50, MSO51, Supplementary Table 4) and selection on complete medium supplemented with G418 or minimal medium lacking uracil, respectively. *HSP104* disruptions were generated by transfection of *Pvu*I-*Bam*HI fragment of pYABL5 (a gift from S. Lindquist) and selection on minimal medium lacking leucine. The *LEU2* marker was subsequently disrupted with *kanMX4* by transfecting a *Bam*HI fragment of SB194 and selecting on YPD+G418. *SUP35* disruptions were generated by transfection of PCR-generated cassettes using pFA6a-His3MX6 as a templated with indicated primers (FP35, FP36, Supplementary Table 4). All disruptions were created in diploid strains and verified by PCR and segregation. [*psi*$^-$][*PIN*$^+$] derivatives were generated by overexpression of Hsp104 in the parental [*PSI*$^+$][*PIN*$^+$] derivative by transfecting plasmid pYS104 (a gift from S. Lindquist), selecting on minimal medium lacking uracil, and counterselecting on 5-FOA. [*psi*$^-$][*pin*$^-$] derivatives were generated by GdnHCl treatment of the parental [*PSI*$^+$][*PIN*$^+$] derivative. [*PIN*$^+$] status was confirmed by analysis of Rnq1 aggregates by SDD-AGE (see Protein Analysis) and by [*PSI*$^+$]-inducibility following overexpression of the prion-determining domain of Sup35 (see [*PSI*$^+$] Induction Studies). pRS30535pNM HA was integrated at the *LEU2* locus by digestion with *Ppu*MI followed by transfection and selection for leucine prototrophy. Protein expression was confirmed by immunoblotting with antiserum specific to HA (see Protein Analysis).

Plasmids

All plasmids used in this study are listed in Supplementary Table 5. SB1184 was constructed by subcloning pCup1-NM-GFP from SLL6442 as an *Xho*I-*Sac*I fragment into *Eag*I-*Sac*I-digested pRS413. The *Xho*I and *Eag*I sites were filled in using T4 ligase (New England BioLabs) prior to cloning. SB1183 was constructed by removing the NM-GFP fragment from SB1184 by digesting with *Bam*HI and *Sac*I, filling in the sites with T4 ligase, and religating.

[PSI$^+$] Induction and Loss Studies

For [*PSI*$^+$] induction promoted by Sup35 overexpression, yeast strains were transfected with SB1183 or SB1184 and plated on minimal medium lacking histidine. Colonies were grown to mid-log phase in minimal medium lacking histidine and in the presence of 40μM $CuSO_4$ to induce expression of NM-GFP for 4 hours. Cells were then harvested by centrifugation and plated on ¼ YPD to assess colony color. For each strain, at least 1000 colonies in at least 10 independent experiments were scored. The frequency of [*PSI*$^+$] induction was determined using a fluctuation test, as previously described.[49] For [*PSI*$^+$] induction

promoted by pre-assembled Sup35 amyloid, the prion-determining domain of Sup35 (NM) was expressed in *E. coli*, purified and assembled into amyloid fibers as previously described[31,78] and transfected into yeast as previously described.[79] Transfectants were plated on YPD to assess colony color. In all cases, [*PSI*$^+$] induction was confirmed by GdnHCl curability. To determine the frequency of spontaneous prion loss, colonies were grown in exponential phase for at least 24 hours before plating on 1/4 YPD to assess colony color. For each strain, at least 1000 colonies in at least 10 independent experiments were scored. The frequency of [*PSI*$^+$] loss was determined using a fluctuation test.

Protein Analysis

Quantitative immunoblotting, SDS-PAGE, semidenaturing agarose gel electrophoresis (SDD-AGE), and SDS-sensitivity experiments were performed as previously described[80] with the following modifications. Protein was transferred to Odyssey Nitrocellulose (LI_COR, Lincoln, NE), and immunoblotting included the secondary antibodies IRDye 800CW Goat anti-Rabbit (LI-COR, Lincoln, NE) for Sup35, Rnq1 and Hsp104, IRDye 680LT Goat anti-Mouse (LI-COR, Lincoln, NE) for Pgk1, and IRDye 680RD Goat anti-Rat (LI-COR, Lincoln, NE). Infrared intensities were quantified using an Odyssey CLx Imaging System (LI-COR, Lincoln, NE). For analysis of seed size, cultures were treated with cycloheximide (10 mg/ml) for the indicated times prior to preparation of lysates and analysis by SDD-AGE. Sucrose gradients were performed as previously described.[53] Anti-Sup35,[60] anti-Rnq1 (a gift of E. Craig, The University of Wisconsin - Madison), anti-Ssa1 (a gift of E. Craig, The University of Wisconsin - Madison), anti-Sis1 (a gift of M. Tuite, The University of Kent), and anti-Hsp104 (Abcam #ab69549) rabbit sera and anti-HA (Roche #11867423001) rat serum were used for immunoblotting. Soluble Rnq1 levels were assessed by sensitivity to disruption with 2% SDS as previously described[81] with the following modifications: lysates were incubated at 37°C prior to analysis by SDS-PAGE and immunoblotting for Rnq1. Levels of aggregated and soluble Sup35 were determined by separation on SDS-PAGE and immunoblotting as previously described.[82] NM-HA immunocapture and immunoblotting were performed as previously described,[60] using anti-HA (Pierce #88837) or anti-MYC (Pierce #88842) magnetic beads.

Rnq1 Propagons

To determine the number of Rnq1 propagons, we exploited the observation that cells can only become [*PSI*$^+$] upon overexpression of Sup35 if they are propagating the [*PIN*$^+$] prion. Specifically, [*psi*$^-$][*PIN*$^+$] strains were transfected with p6442 or p6430 and were then grown in minimal medium lacking uracil to mid-log phase before plating on minimal medium lacking uracil and containing 3mM GdnHCl. Single colonies were picked by micromanipulation and allowed to grow for 2–3 days at 30°C. Individual colonies were resuspended in water, plated on minimal medium lacking uracil and containing 50μM $CuSO_4$ and grown for 4 days at 30°C to allow overexpression of NM-GFP. Cells were then replicated plated onto YPD and allowed to grow for 4 days before the number of white [*PSI*$^+$] colonies, corresponding to the number of [*PIN*$^+$] propagons, were counted. Control experiments where single colonies were picked on minimal medium not containing 3mM GdnHCl show > 95% [*PSI*$^+$] induction, while strains transfected with p6430 had no [*PSI*$^+$] appearance.

Mathematical Modeling

Fiber transfection experiments were analyzed to determine the number of fibers necessary to induce the [*PSI*$^+$] state by scaling out both the concentration of fibers and the concentration of fibers taken up by cells as previously described.[31] To analyze the forces impacting transitions in prion state, we use two different mathematical formulations of prion aggregate dynamics. These formulations do not consider the *de novo* formation of seeds, but rather the fate of introduced aggregates based on nucleated polymerization dynamics, as previously described.[5] To develop mathematical predictions to compare with experiments on yeast strains with an existing prion state (i.e. stable aggregate distribution), we use an established deterministic model to depict the time evolution of the concentration of introduced biochemical species according to the rates of monomer synthesis (a), degradation (μ), monomer conversion to the prion state (b), and aggregate fragmentation (g) through a system of differential equations, as previously described.[5] To develop mathematical predictions on the fate of an aggregate introduced into a single cell during the course of the first cell division, we developed a novel stochastic model of prion aggregate dynamics. We use the chemical master equation to determine the probability that an aggregate of minimal stable size introduced to a newly born cell will evolve under nucleated polymerization dynamics to create two aggregates at or above the minimal stable size before cell division. This represents the minimum requirement for persistence of the prion state. A full description of these models is available in Supplementary Note 1.

Reporting Summary

Further information on experimental design is available in the Nature Research Reporting Summary linked to this article.

Code Availability

Code for the stochastic model of aggregate persistence is available at https://doi.org/10.6071/M33T08

Data Availability

Source data for figures 1b–e, 1g, 2b, 2d–f, 4b and extended data figures 1a–b, 2a–c, and 2d are available with the paper online.

Extended Data

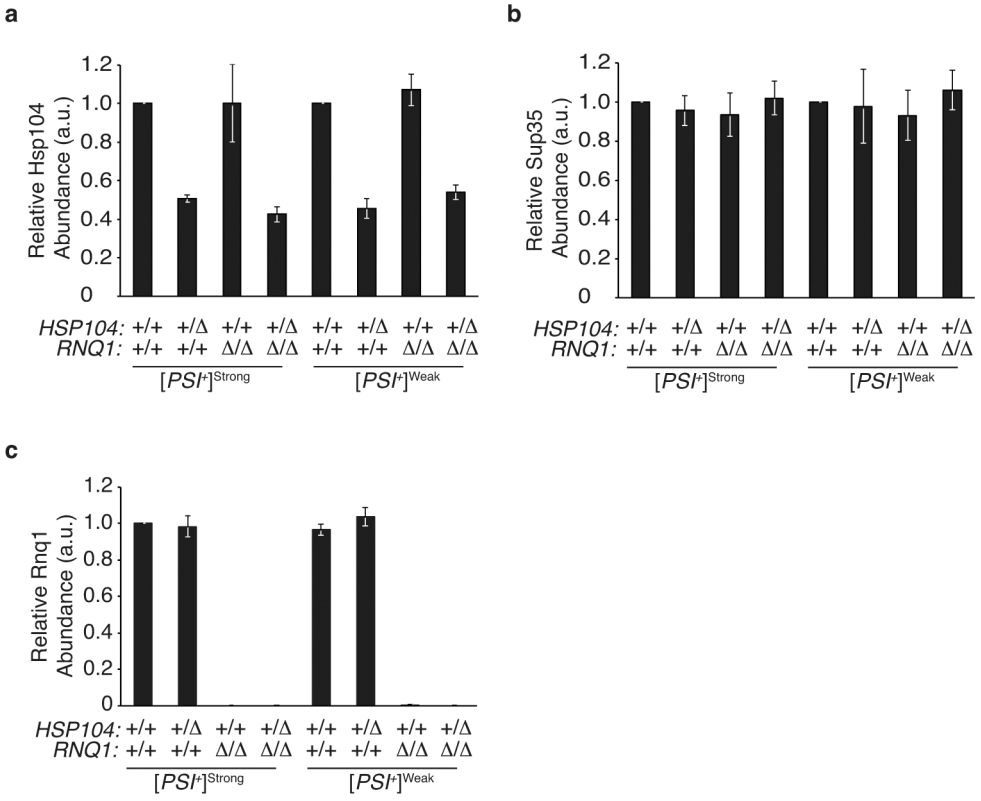

Extended Data Fig. 1. Protein abundance for strains with heterozygous disruptions of *HSP104* and/or *RNQ1*

The relative levels of Hsp104 (**a**), Sup35 (**b**), and Rnq (**c**) in lysates from diploid yeast strains analyzed in Fig. 1 e, f, g were determined by SDS-PAGE and immunoblotting with specific antisera. Strains carried wildtype (+/+), heterozygous (+/Δ), or homozygous (Δ/Δ) disruptions of *HSP104* or *RNQ*1 and the indicated variant of [*PSI*$^{+}$]. Protein levels are expressed relative to the protein levels in wildtype version of the same prion strain (i.e. [*PSI*$^{+}$]^{Strong} or [*PSI*$^{+}$]^{Weak}) in arbitrary units (a.u.). Data are mean and s.d. from 3 independent experiments performed with independent cultures. Data for the graphs in panels a-b are available as source data.

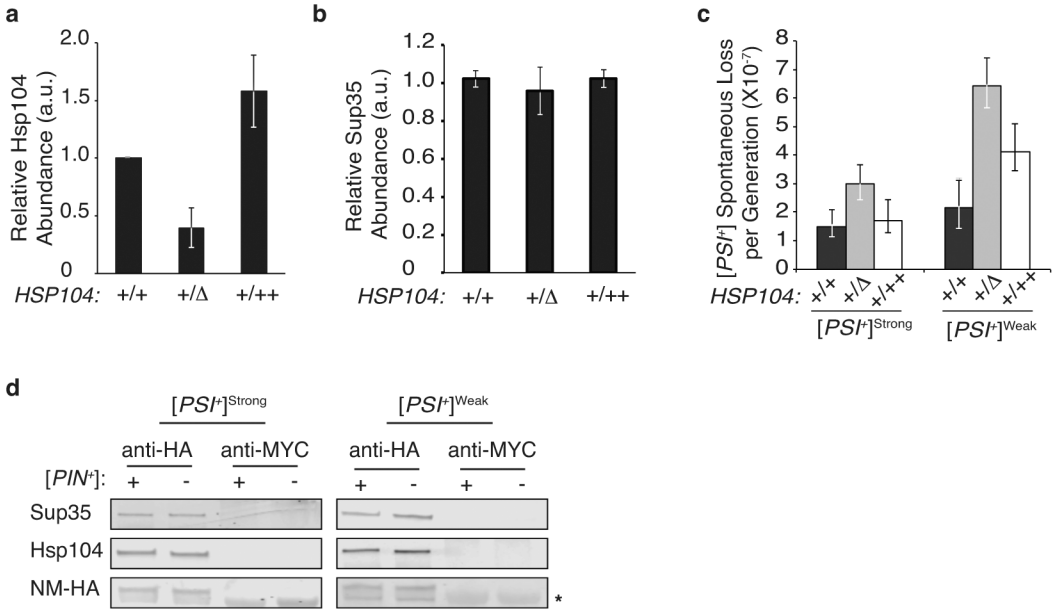

Extended Data Fig. 2. Hsp104 abundance, availability and association with Sup35 in strains with varying copy number or propagating [*PIN*$^+$]

The relative levels of Hsp104 (**a**) and Sup35 (**b**) in lysates from diploid yeast strains used to determine the frequency of [*PSI*$^+$] appearance in response to transient overexpression of the Sup35 prion domain (Fig. 2c) were determined by SDS-PAGE and immunoblotting with specific antisera. Strains carried wildtype (+/+), heterozygous disruptions of *HSP104* (+/Δ), or an extra copy of *HSP104* (+/++). Protein levels are expressed relative to wildtype in arbitrary units (a.u.). Data are mean and s.d. from 3 independent experiments performed with independent cultures. **c**. The frequency of spontaneous loss of the indicated [*PSI*$^+$] variant was determined in yeast strains carrying wildtype (+/+, black), heterozygous disruptions of *HSP104* (+/Δ, gray), or an extra copy of *HSP104* (+/++). Data shown are means; error bars represent 95% confidence intervals from ten independent cultures. **d**. Representative immunoblots of SDS-PAGE gels following immunocapture of NM-HA from lysates isolated from the indicated [*PSI*$^+$] variant using either specific (anti-HA) or non-specific (anti-MYC) beads. Both [*PIN*$^+$] (+) and [*pin*$^-$] (−) strains were analyzed for capture of NM-HA and co-capture of Sup35 and Hsp104, using specific anti-sera. A non-specific band cross-reacting with the HA antiserum is indicated (*). Data for the graphs in panels a-c and uncropped images for panel d are available as source data.

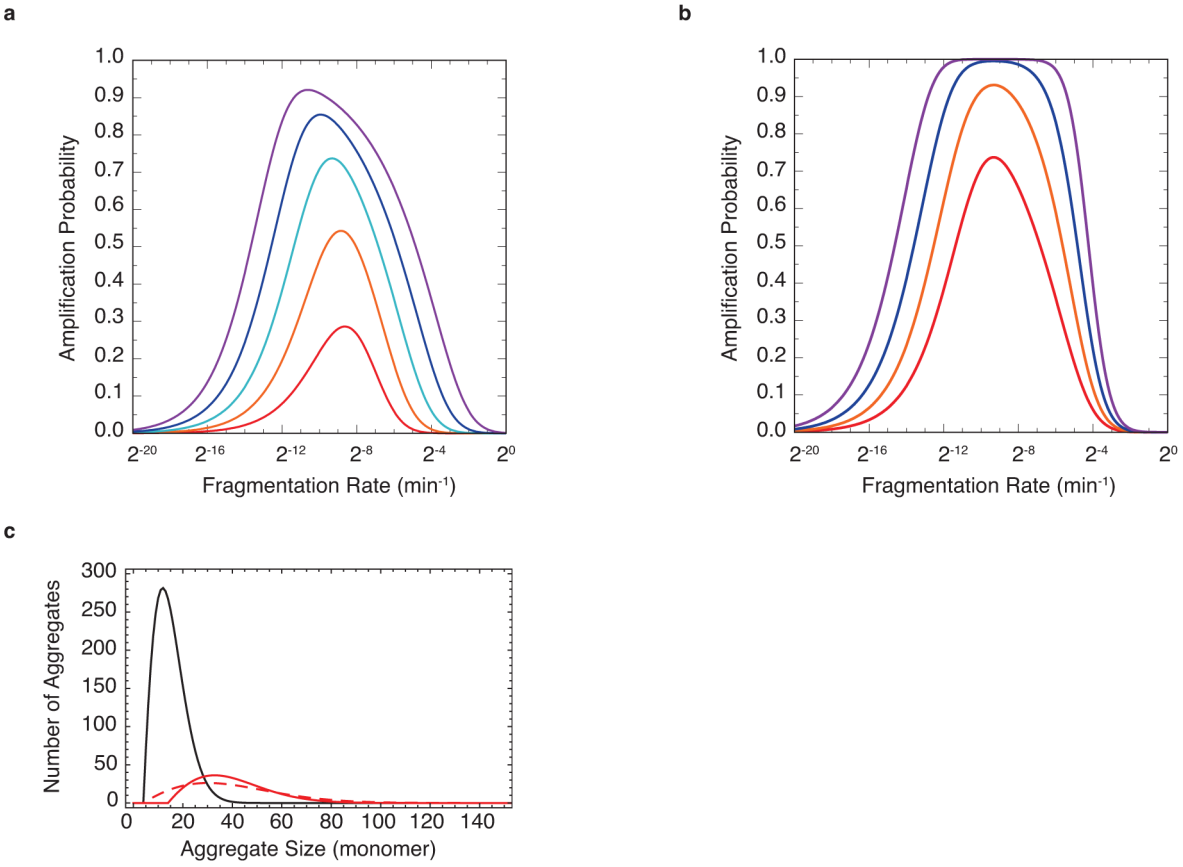

Extended Data Fig. 3. Aggregate amplification probabilities and size distributions

A stochastic persistence model of Sup35 aggregate dynamics *in vivo* determines the probability of amplification of a single Sup35 aggregate as a function of fragmentation rate with Sup35 expression levels (**a**) at 25% (red), 50% (orange), 100% (teal), 200% (blue) or 400% (purple) or Sup35 aggregate numbers (**b**) of one (red), two (orange), four (blue) or eight (purple) for [*PSI*$^{+}$]$^{\text{Strong}}$ with a seed size of five. **c**. Aggregate size distributions for [*PSI*$^{+}$]$^{\text{Strong}}$ with a seed size of five (solid black), [*PSI*$^{+}$]$^{\text{Weak}}$ with a seed size of five (dashed red), or [*PSI*$^{+}$]$^{\text{Weak}}$ with a seed size of fifteen (solid red) are shown.

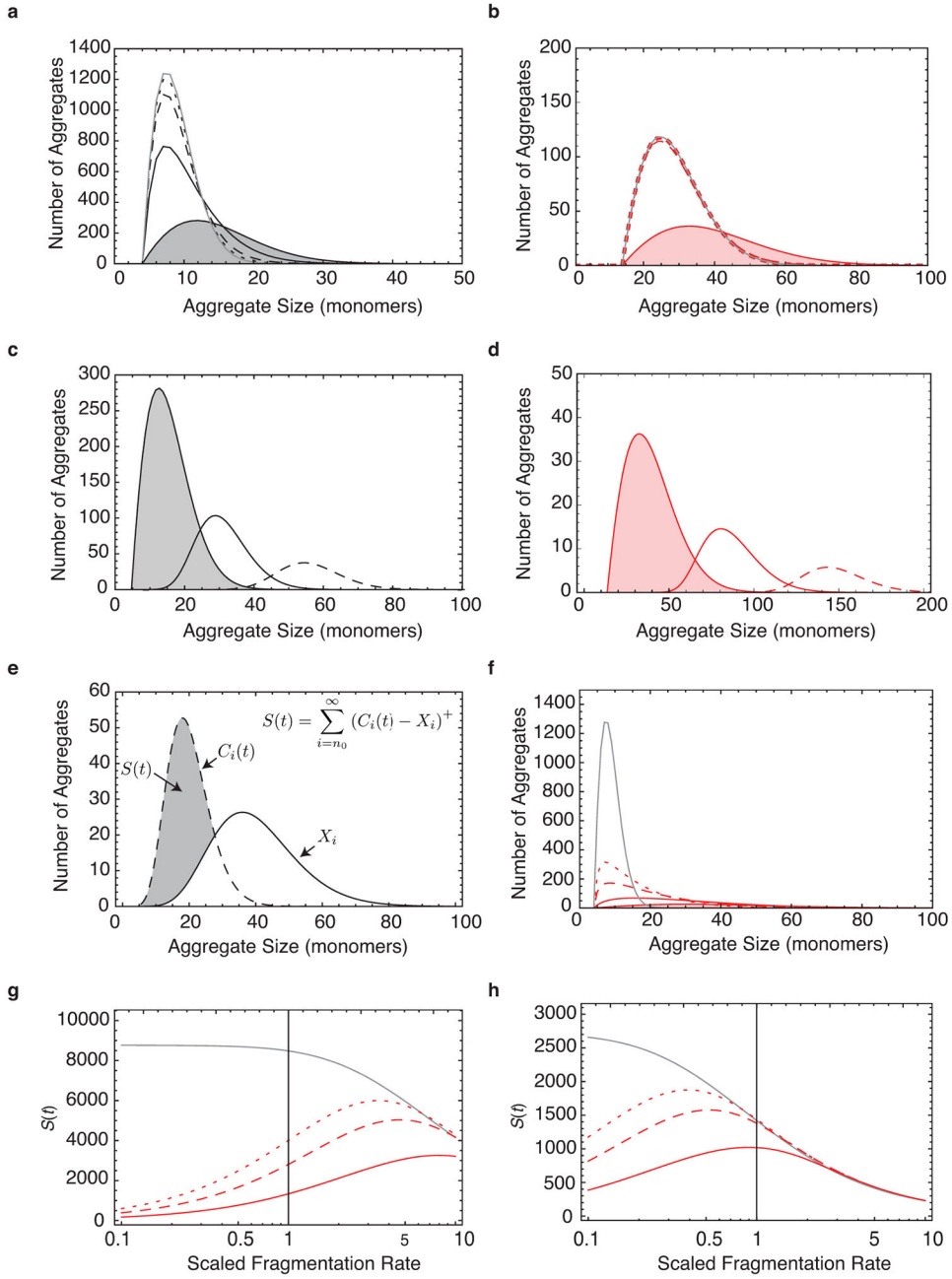

Extended Data Fig. 4. Aggregate size distribution shifts in response to experimental perturbation

The aggregate size distributions revealed by our deterministic model (shaded) shift in response to inhibition of Sup35 synthesis (**a, b**) or Hsp104-mediated fragmentation (**c, d**) after 90 min (solid, unshaded),180 min (dashed, unshaded), 270 min (dotted, unshaded) or at its steady-state (gray, unshaded) for strains propagating $[PSI^+]^{Strong}$ with a seed size of 5 (**a, c**) or $[PSI^+]^{Weak}$ with a seed size of fifteen (**b, d**). **e.** The distribution of aggregate sizes before (X_i, solid black) and after ($C_i(t)$, dashed black) t minutes of inhibition of Sup35 synthesis is shown. The shift in the size distribution, $S(t)$, is quantified as the area between the curves when $C_i(t) > X_i$ (shaded area). **f.** The size distribution of Sup35 aggregates from a

strain propagating [*PSI*$^{+}$]^{Weak} with a seed size of five (shaded) shifts upon inhibition of Sup35 synthesis for 90 min (solid, unshaded), 180 min (dashed, unshaded), 270 min (dotted, unshaded) or at its steady-state (gray, unshaded). **g.** and **h.** The shifts in aggregate size distribution over a range of fragmentation and conversion rates that match the steady-state soluble level of Sup35 were monitored at 90 min (solid), 180 min (dashed), 270 min (dotted) and steady-state (gray) for a strain propagating [*PSI*$^{+}$]^{Weak} with a seed size of five (**g**) or fifteen (**h**). The x-axis shows the fragmentation rate scaled to the strain-specific value in Supplementary Table 2 (vertical black line). While [*PSI*+]^{Weak} with a seed size of five (**g**) shifts slowly to its steady-state distribution, [*PSI*$^{+}$]^{Weak} with a seed size of fifteen (**h**) rapidly reaches is steady-state distribution, matching our empirical observations (Fig. 4a).

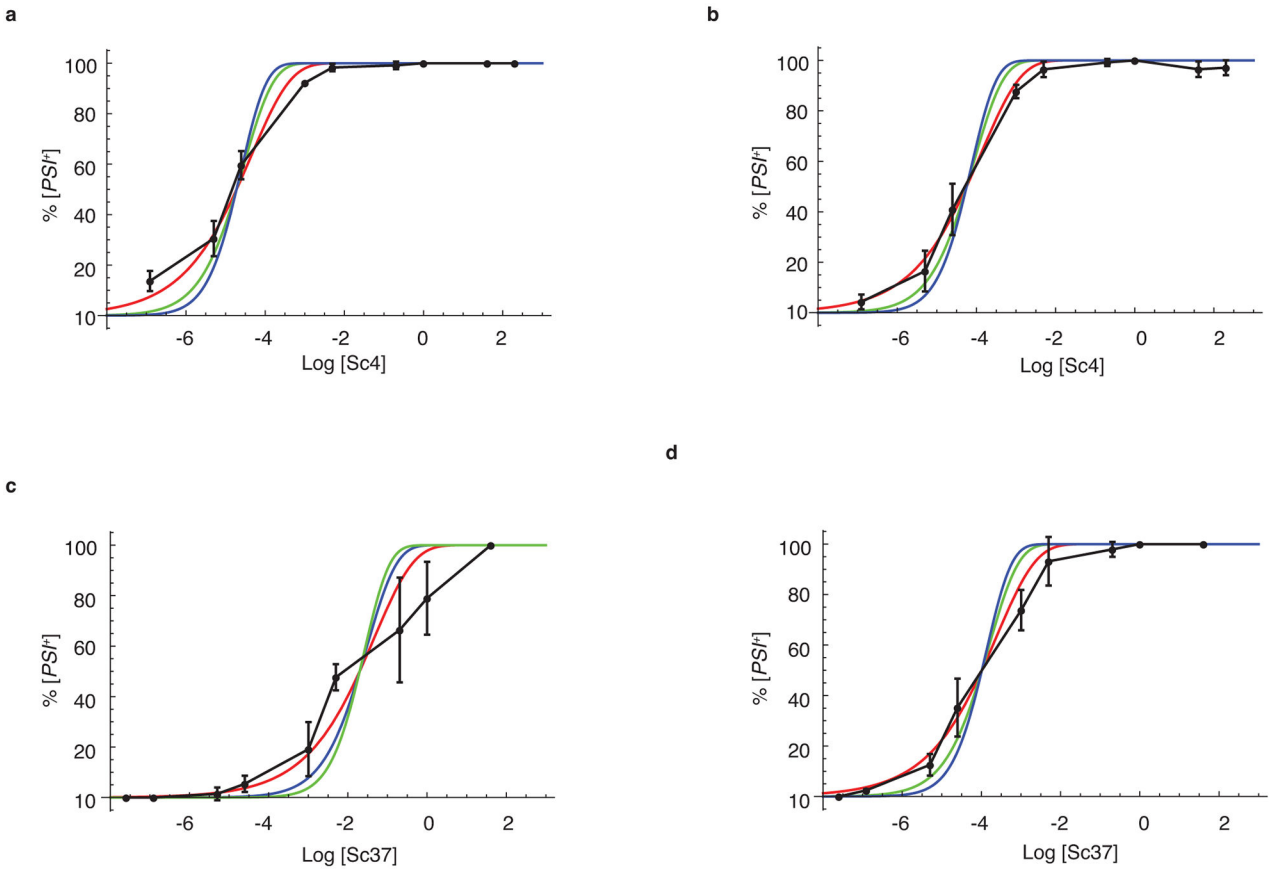

Extended Data Fig. 5. Fiber transfection fitting

Fiber transfection experiments from Fig. 1 were fit mathematically to determine the number of fibers required to induce a stable [*PSI*$^{+}$] state. Shown are the observations (black) and fits for fibers of the prion domain of Sup35 assembled at 4°C (Sc4) or at 37°C (Sc37) in [*pin*$^{-}$] (**a, c**) or [*PIN*$^{+}$] (**b, d**) yeast strains to a model of one (red), two (green), or three (blue) fibers. Data shown are means and s.d. from at least two independent experiments performed with independent cultures.

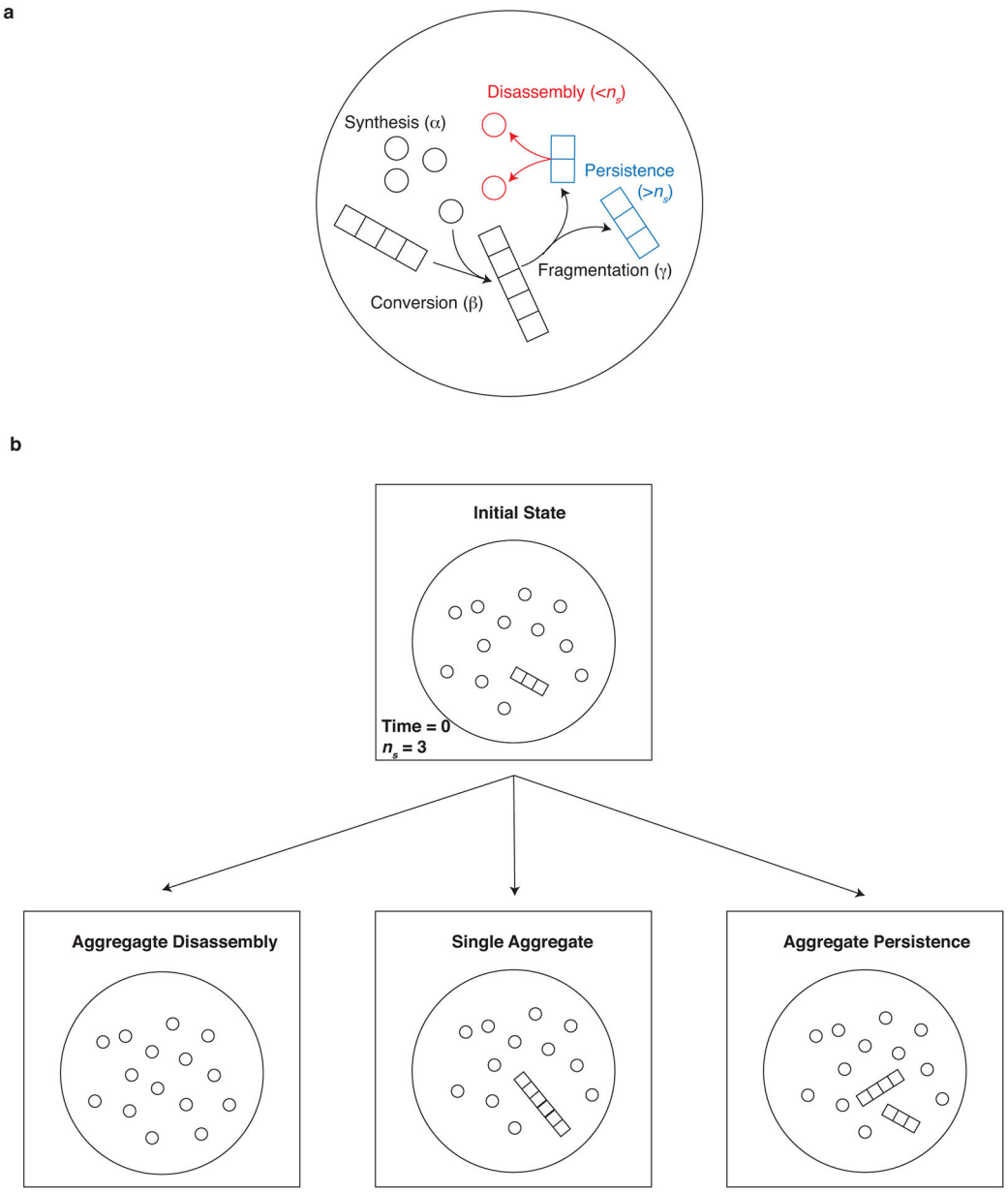

Extended Data Fig. 6. Schematics of mathematical models

a. Schematic of nucleated polymerization dynamics used in the mathematical models. Non-prion state Sup35 (circle) is synthesized at rate α and can join either end an amyloid aggregate of Sup35 (polymer of squares) at a conversion rate β. Amyloid aggregates are fragmented at rate γ at the interface between any two monomers. If the resulting two aggregates are both greater in size than the minimum seed (n_s), the amyloid state persists (blue); if either aggregate is smaller in size than n_s, it will disassemble into non-prion state Sup35 (red). **b.** The stochastic persistence model calculates the probability of each of three outcomes, relative to cell division, upon the introduction of a single aggregate of minimal size under nucleated polymerization dynamics: aggregate disassembly, retention of a single

aggregate, and aggregate persistence (i.e. the creation of two aggregates greater in size than n_s).

Supplementary Material

Refer to Web version on PubMed Central for supplementary material.

Acknowledgements

We thank S. Lindquist (MIT) and E. Craig (The University of Wisconsin – Madison) for reagents and J. Laney and members of the Serio and Sindi groups for helpful discussions and comments on the manuscript. This research was sponsored in part by the Joint DMS/NIGMS Initiative to Support Research at the Interface of the Biological and Mathematical Sciences (R01GM126548 to SSS), NSF-INSPIRE (1344279 to SSS and JKD), and NIH/NIGMS (F32 GM096582 to JV, R35 GM118042 to TRS) and with support from NIH/NIGMS to TMB (T32GM008659).

References

1. Tuite MF & Serio TR The prion hypothesis: from biological anomaly to basic regulatory mechanism. Nat Rev Mol Cell Biol 11, 823–833 (2010). [PubMed: 21081963]
2. Knowles TPJ, Vendruscolo M & Dobson CM The amyloid state and its association with protein misfolding diseases. Nat Rev Mol Cell Biol 15, 384–396 (2014). [PubMed: 24854788]
3. Serio TR [*PIN*$^+$]ing down the mechanism of prion appearance. FEMS Yeast Res. 18, 924 (2018).
4. Masel J, Jansen VA & Nowak MA Quantifying the kinetic parameters of prion replication. Biophys Chem 77, 139–152 (1999). [PubMed: 10326247]
5. Masel J & Jansen VA The measured level of prion infectivity varies in a predictable way according to the aggregation state of the infectious agent. Biochim Biophys Acta 1535, 164–173 (2001). [PubMed: 11342005]
6. Knowles TP et al. An analytical solution to the kinetics of breakable filament assembly. Science 326, 1533–1537 (2009). [PubMed: 20007899]
7. Gaspar R et al. Secondary nucleation of monomers on fibril surface dominates α-synuclein aggregation and provides autocatalytic amyloid amplification. Q. Rev. Biophys 50, e6 (2017). [PubMed: 29233218]
8. Jarrett JT & Lansbury PT Seeding ‘one-dimensional crystallization’ of amyloid: a pathogenic mechanism in Alzheimer’s disease and scrapie? Cell 73, 1055–1058 (1993). [PubMed: 8513491]
9. Come JH, Fraser PE & Lansbury PT A kinetic model for amyloid formation in the prion diseases: importance of seeding. Proc Natl Acad Sci U S A 90, 5959–5963 (1993). [PubMed: 8327467]
10. Nowak MA, Krakauer DC, Klug A & May RM Prion infection dynamics. Integrative Biology: Issues, News, and Reviews 1, 3–15 (1998).
11. Powers ET, Morimoto RI, Dillin A, Kelly JW & Balch WE Biological and chemical approaches to diseases of proteostasis deficiency. Annu Rev Biochem 78, 959–991 (2009). [PubMed: 19298183]
12. Koga H, Kaushik S & Cuervo AM Protein homeostasis and aging: The importance of exquisite quality control. Ageing Res. Rev 10, 205–215 (2011). [PubMed: 20152936]
13. Derkatch IL, Bradley ME, Hong JY & Liebman SW Prions affect the appearance of other prions: the story of [*PIN*$^+$]. Cell 106, 171–182 (2001). [PubMed: 11511345]
14. Osherovich LZ & Weissman JS Multiple Gln/Asn-rich prion domains confer susceptibility to induction of the yeast [*PSI*$^+$] prion. Cell 106, 183–194 (2001). [PubMed: 11511346]
15. Gidalevitz T, Ben-Zvi A, Ho KH, Brignull HR & Morimoto RI Progressive disruption of cellular protein folding in models of polyglutamine diseases. Science 311, 1471–1474 (2006). [PubMed: 16469881]
16. Tyedmers J, Madariaga ML & Lindquist S Prion switching in response to environmental stress. PLoS Biol 6, e294 (2008). [PubMed: 19067491]
17. Cox BS [*PSI*], a cytoplasmic suppressor of super-suppression in yeast. Heredity 20, 505–521 (1965).

18. Doel SM, McCready SJ, Nierras CR & Cox BS The dominant PNM2- mutation which eliminates the psi factor of *Saccharomyces cerevisiae* is the result of a missense mutation in the *SUP35* gene. Genetics 137, 659–670 (1994). [PubMed: 8088511]
19. Ter-Avanesyan MD, Dagkesamanskaya AR, Kushnirov VV & Smirnov VN The *SUP35* omnipotent suppressor gene is involved in the maintenance of the non-Mendelian determinant [*PSI*$^{+}$] in the yeast *Saccharomyces cerevisiae*. Genetics 137, 671–676 (1994). [PubMed: 8088512]
20. Chernoff YO, Lindquist SL, Ono B, Inge-Vechtomov SG & Liebman SW Role of the chaperone protein Hsp104 in propagation of the yeast prion-like factor [*PSI*$^{+}$]. Science 268, 880–884 (1995). [PubMed: 7754373]
21. Patino MM, Liu JJ, Glover JR & Lindquist S Support for the prion hypothesis for inheritance of a phenotypic trait in yeast. Science 273, 622–626 (1996). [PubMed: 8662547]
22. Paushkin SV, Kushnirov VV & Smirnov VN Propagation of the yeast prion-like [*PSI*$^{+}$] determinant is mediated by oligomerization of the *SUP35*-encoded polypeptide chain release factor. EMBO J 15, 3127–3134 (1996). [PubMed: 8670813]
23. Glover JR et al. Self-seeded fibers formed by Sup35, the protein determinant of [*PSI*$^{+}$], a heritable prion-like factor of *S. cerevisiae*. Cell 89, 811–819 (1997). [PubMed: 9182769]
24. King CY et al. Prion-inducing domain 2–114 of yeast Sup35 protein transforms in vitro into amyloid-like filaments. Proc Natl Acad Sci U S A 94, 6618–6622 (1997). [PubMed: 9192614]
25. Paushkin SV, Kushnirov VV, Smirnov VN & Ter-Avanesyan MD In vitro propagation of the prion-like state of yeast Sup35 protein. Science 277, 381–383 (1997). [PubMed: 9219697]
26. Derkatch IL, Bradley ME, Zhou P, Chernoff YO & Liebman SW Genetic and environmental factors affecting the de novo appearance of the [*PSI*$^{+}$] prion in *Saccharomyces cerevisiae*. Genetics 147, 507–519 (1997). [PubMed: 9335589]
27. Sarell CJ, Stockley PG & Radford SE Assessing the causes and consequences of co-polymerization in amyloid formation. Prion 7, 359–368 (2013). [PubMed: 24025483]
28. Krebs MRH, Morozova-Roche LA, Daniel K & Dobson CM Observation of sequence specificity in the seeding of protein amyloid fibrils. Protein Sci 13, 1933–1938 (2004). [PubMed: 15215533]
29. Resende C et al. The *Candida albicans* Sup35p protein (CaSup35p): function, prion-like behaviour and an associated polyglutamine length polymorphism. Microbiology 148, 1049–1060 (2002). [PubMed: 11932450]
30. Santoso A, Chien P, Osherovich LZ & Weissman JS Molecular basis of a yeast prion species barrier. Cell 100, 277–288 (2000). [PubMed: 10660050]
31. Tanaka M, Collins SR, Toyama BH & Weissman JS The physical basis of how prion conformations determine strain phenotypes. Nature 442, 585–589 (2006). [PubMed: 16810177]
32. Derdowski A, Sindi SS, Klaips CL, DiSalvo S & Serio TR A size threshold limits prion transmission and establishes phenotypic diversity. Science 330, 680–683 (2010). [PubMed: 21030659]
33. Dickinson AG, Fraser H, Meikle VM & Outram GW Competition between different scrapie agents in mice. Nature: New biology 237, 244–245 (1972). [PubMed: 4624846]
34. Dickinson AG Host-pathogen interactions in scrapie. Genetics 79 Suppl, 387–395 (1975). [PubMed: 807505]
35. Manuelidis L Vaccination with an attenuated Creutzfeldt-Jakob disease strain prevents expression of a virulent agent. Proc Natl Acad Sci U S A 95, 2520–2525 (1998). [PubMed: 9482918]
36. Bartz JC et al. Prion interference is due to a reduction in strain-specific PrPSc levels. J Virol 81, 689–697 (2007). [PubMed: 17079313]
37. Tanaka M et al. Conformational variations in an infectious protein determine prion strain differences. Nature 428, 323–328 (2004). [PubMed: 15029196]
38. King C-Y Transformation of yeast by infectious prion particles. Methods 39, 68–71 (2006). [PubMed: 16759879]
39. Song Y et al. Role for Hsp70 chaperone in *Saccharomyces cerevisiae* prion seed replication. Eukaryot Cell 4, 289–297 (2005). [PubMed: 15701791]
40. Satpute-Krishnan P, Langseth SX & Serio TR Hsp104-dependent remodeling of prion complexes mediates protein-only inheritance. PLoS Biol 5, e24 (2007). [PubMed: 17253904]

41. Higurashi T, Hines JK, Sahi C, Aron R & Craig EA Specificity of the J-protein Sis1 in the propagation of 3 yeast prions. Proc Natl Acad Sci U S A 105, 16596–16601 (2008). [PubMed: 18955697]
42. Tipton KA, Verges KJ & Weissman JS In vivo monitoring of the prion replication cycle reveals a critical role for Sis1 in delivering substrates to Hsp104. Mol Cell 32, 584–591 (2008). [PubMed: 19026788]
43. Pei F, DiSalvo S, Sindi SS & Serio TR A dominant-negative mutant inhibits multiple prion variants through a common mechanism. PLoS Genet 13, e1007085 (2017). [PubMed: 29084237]
44. DiSalvo S, Derdowski A, Pezza JA & Serio TR Dominant prion mutants induce curing through pathways that promote chaperone-mediated disaggregation. Nat Struct Mol Biol 18, 486–492 (2011). [PubMed: 21423195]
45. Klaips CL, Hochstrasser ML, Langlois CR & Serio TR Spatial quality control bypasses cell-based limitations on proteostasis to promote prion curing. Elife 3, 1751 (2014).
46. Sondheimer N & Lindquist S Rnq1: An Epigenetic Modifier of Protein Function in Yeast. Mol Cell 5, 163–172 (2000). [PubMed: 10678178]
47. Derkatch IL, Chernoff YO, Kushnirov VV, Inge-Vechtomov SG & Liebman SW Genesis and variability of [*PSI*] prion factors in *Saccharomyces cerevisiae*. Genetics 144, 1375–1386 (1996). [PubMed: 8978027]
48. Bagriantsev S & Liebman SW Specificity of prion assembly in vivo. [PSI^+] and [PIN^+] form separate structures in yeast. J Biol Chem 279, 51042–51048 (2004). [PubMed: 15465809]
49. Lancaster AK, Bardill JP, True HL & Masel J The spontaneous appearance rate of the yeast prion [PSI^+] and its implications for the evolution of the evolvability properties of the [PSI^+] system. Genetics 184, 393–400 (2010). [PubMed: 19917766]
50. Zhou P, Derkatch IL & Liebman SW The relationship between visible intracellular aggregates that appear after overexpression of Sup35 and the yeast prion-like elements [PSI^+] and [PIN^+]. Mol Microbiol 39, 37–46 (2001). [PubMed: 11123686]
51. Borchsenius AS, Muller S, Newnam GP, Inge-Vechtomov SG & Chernoff YO Prion variant maintained only at high levels of the Hsp104 disaggregase. Current genetics 49, 21–29 (2006). [PubMed: 16307272]
52. Kryndushkin DS, Engel A, Edskes H & Wickner RB Molecular chaperone Hsp104 can promote yeast prion generation. Genetics 188, 339–348 (2011). [PubMed: 21467567]
53. Pezza JA, Villali J & Serio TR Amyloid-associated activity contributes to the severity and toxicity of a prion phenotype. Nat Comm 5, 4384 (2014).
54. Sharma J & Liebman SW Exploring the basis of [PIN^+] variant differences in [PSI^+] induction. J Mol Biol 425, 3046–3059 (2013). [PubMed: 23770111]
55. Gillespie DT The chemical Langevin equation. J Chem Phys 113, 297–306 (2000).
56. Ferrone FA, Hofrichter J & Eaton WA Kinetics of sickle hemoglobin polymerization. II. A double nucleation mechanism. J Mol Biol 183, 611–631 (1985). [PubMed: 4020873]
57. Wegrzyn RD, Bapat K, Newnam GP, Zink AD & Chernoff YO Mechanism of prion loss after Hsp104 inactivation in yeast. Mol Cell Biol 21, 4656–4669 (2001). [PubMed: 11416143]
58. Kryndushkin DS, Ter-Avanesyan MD & Kushnirov VV Yeast [PSI^+] prion aggregates are formed by small Sup35 polymers fragmented by Hsp104. J Biol Chem 278, 49636–49643 (2003). [PubMed: 14507919]
59. Liu JJ & Lindquist S Oligopeptide-repeat expansions modulate 'protein-only' inheritance in yeast. Nature 400, 573–576 (1999). [PubMed: 10448860]
60. Langlois CR, Pei F, Sindi SS & Serio TR Distinct Prion Domain Sequences Ensure Efficient Amyloid Propagation by Promoting Chaperone Binding or Processing *In Vivo*. PLoS Genet 12, e1006417 (2016). [PubMed: 27814358]
61. Hofrichter J, Ross PD & Eaton WA Kinetics and mechanism of deoxyhemoglobin S gelation: a new approach to understanding sickle cell disease. Proc Natl Acad Sci U S A 71, 4864–4868 (1974). [PubMed: 4531026]
62. Yang Z, Hong JY, Derkatch IL & Liebman SW Heterologous gln/asn-rich proteins impede the propagation of yeast prions by altering chaperone availability. PLoS Genet 9, e1003236 (2013). [PubMed: 23358669]

63. Arslan F, Hong JY, Kanneganti V, Park S-K & Liebman SW Heterologous aggregates promote de novo prion appearance via more than one mechanism. PLoS Genet 11, e1004814 (2015). [PubMed: 25568955]
64. Bradley ME, Edskes HK, Hong JY, Wickner RB & Liebman SW Interactions among prions and prion 'strains' in yeast. Proc Natl Acad Sci U S A 99 Suppl 4, 16392–16399 (2002). [PubMed: 12149514]
65. Mathur V, Hong JY & Liebman SW Ssa1 overexpression and [*PIN*$^+$] variants cure [*PSI*$^+$] by dilution of aggregates. J Mol Biol 390, 155–167 (2009). [PubMed: 19422835]
66. Westergard L & True HL Extracellular environment modulates the formation and propagation of particular amyloid structures. Mol Microbiol 92, 698–715 (2014). [PubMed: 24628771]
67. Khan T et al. Quantifying Nucleation In Vivo Reveals the Physical Basis of Prion-like Phase Behavior. Mol Cell 71, 155–168.e7 (2018). [PubMed: 29979963]
68. Park K-W, Hahn J-S, Fan Q, Thiele DJ & Li L *De novo* appearance and 'strain' formation of yeast prion [*PSI*$^+$] are regulated by the heat-shock transcription factor. Genetics 173, 35–47 (2006). [PubMed: 16452152]
69. Stein KC & True HL Extensive diversity of prion strains is defined by differential chaperone interactions and distinct amyloidogenic regions. PLoS Genet 10, e1004337 (2014). [PubMed: 24811344]
70. Dulle JE & True HL Low activity of select Hsp104 mutants is sufficient to propagate unstable prion variants. Prion 7, 394–403 (2013). [PubMed: 24064980]
71. Dulle JE, Stein KC & True HL Regulation of the Hsp104 middle domain activity is critical for yeast prion propagation. PloS one 9, e87521 (2014). [PubMed: 24466354]
72. Bradley ME & Liebman SW Destabilizing interactions among [*PSI*$^+$] and [*PIN*$^+$] yeast prion variants. Genetics 165, 1675–1685 (2003). [PubMed: 14704158]
73. Stein KC, Bengoechea R, Harms MB, Weihl CC, & True HL Myopathy-causing mutations in an HSP40 chaperone disrupt processing of specific client conformers. J Biol Chem 289, 21120–21130 (2014). [PubMed: 24920671]
74. Zampieri M, Legname G & Altafini C Investigating the conformational stability of prion strains through a kinetic replication model. PLoS Comput. Biol 5, e1000420 (2009). [PubMed: 19578427]
75. Sun Y et al. Conformational stability of PrP amyloid fibrils controls their smallest possible fragment size. J Mol Biol 376, 1155–1167 (2008). [PubMed: 18206163]
76. Gao X et al. Human Hsp70 Disaggregase Reverses Parkinson's-Linked α-Synuclein Amyloid Fibrils. Mol Cell 59, 781–793 (2015). [PubMed: 26300264]
77. Kirstein J et al. In vivo properties of the disaggregase function of J-proteins and Hsc70 in *Caenorhabditis elegans* stress and aging. Aging Cell 16, 1414–1424 (2017). [PubMed: 29024389]
78. Serio TR, Cashikar AG, Moslehi JJ, Kowal AS & Lindquist SL Yeast prion [*PSI*$^+$] and its determinant, Sup35p. Meth. Enzymol 309, 649–673 (1999). [PubMed: 10507053]
79. Tanaka M A protein transformation protocol for introducing yeast prion particles into yeast. Methods Enzymol 470, 681–693 (2010). [PubMed: 20946831]
80. Pezza JA et al. The NatA acetyltransferase couples Sup35 prion complexes to the [*PSI*$^+$] phenotype. Mol Biol Cell 20, 1068–1080 (2009). [PubMed: 19073888]
81. Satpute-Krishnan P & Serio TR Prion protein remodelling confers an immediate phenotypic switch. Nature 437, 262–265 (2005). [PubMed: 16148935]
82. Kushnirov VV, Alexandrov IM, Mitkevich OV, Shkundina IS & Ter-Avanesyan MD Purification and analysis of prion and amyloid aggregates. Methods 39, 50–55 (2006). [PubMed: 16774835]

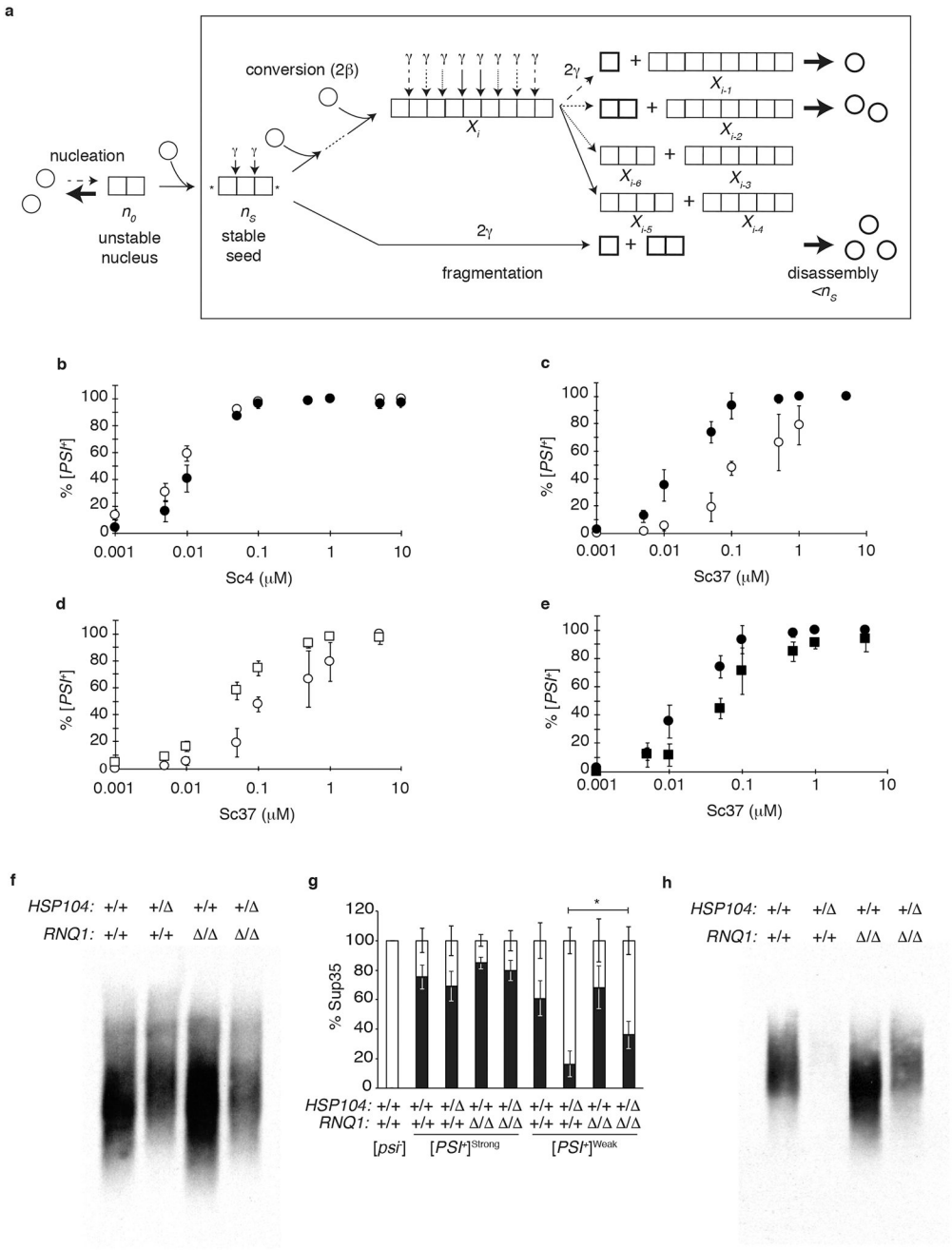

Fig 1.

[*PIN*$^{+}$] and deletion of Hsp104 combine to impact appearance and propagation of [*PSI*$^{+}$]^{Weak}. **a.** Native monomer (circle) spontaneously and rarely (dashed arrow) associates to form a nucleus of size n_0, the rate-limiting step for amyloid formation. The nucleus is thermodynamically unstable (solid, heavy back arrow), and subsequent addition of monomers through favorable associations ultimately creates a stable seed of minimum size n_s. The seed can grow at a rate that is double the single-site conversion rate (2β) because monomers can add to either end of the aggregate (*). The seed or any larger aggregate may be fragmented at any monomer junction (down arrows) at a single-site fragmentation rate

(γ). Any single fragmentation event will produce two aggregates; note that two fragmentation sites on the same aggregate can yield the same-size products (downward arrows of the same style); thus, aggregates of any given size will be produced at a rate that is double the single-site fragmentation rate (2γ). The products of fragmentation have two fates: aggregates larger in size than n_s are stable (black squares); aggregates smaller than n_s (thick black square) spontaneously disassemble into monomers (thick circles). In this work, we only consider the dynamics of aggregates at or above the size of the minimum stable seed (box). **b–e** Amyloid fibers of the Sup35 prion-determining domain assembled at 4°C (Sc4; **b**) or at 37°C (Sc37; **c, d, e**) were transfected at the indicated concentrations (μM) into [*PIN*$^+$] (black circles), [*pin*$^-$] (open circles), [*pin*$^-$] +/*ΔHSP104* (open square), or [*PIN*$^+$] +/*ΔHSP104* (black square) yeast before plating and scoring for conversion to [*PSI*$^+$]. Data shown are means and s.d. from at least two independent experiments performed with independent cultures. f–h. Analyses of lysates from [*PSI*$^+$]^{Strong} (**f**) or [*PSI*$^+$]^{Weak} (**h**) diploid yeast strains with wildtype (+/+), heterozygous (+/Δ), or homozygous (Δ/Δ) disruptions of *HSP104* or *RNQ1* were analyzed by SDD-AGE and immunoblotting for Sup35. Immunoblots shown are representative of three independent experiments performed with independent cultures. **g.** Graph shows the fraction of soluble (open bars) and aggregated (black bars) Sup35 in lysates from the indicated strains. Data are mean and s.d. from 3 independent experiments performed with independent cultures; *p<0.048 by two-tailed Student's t-test. Data for graphs in panels b-e and g are available as source data.

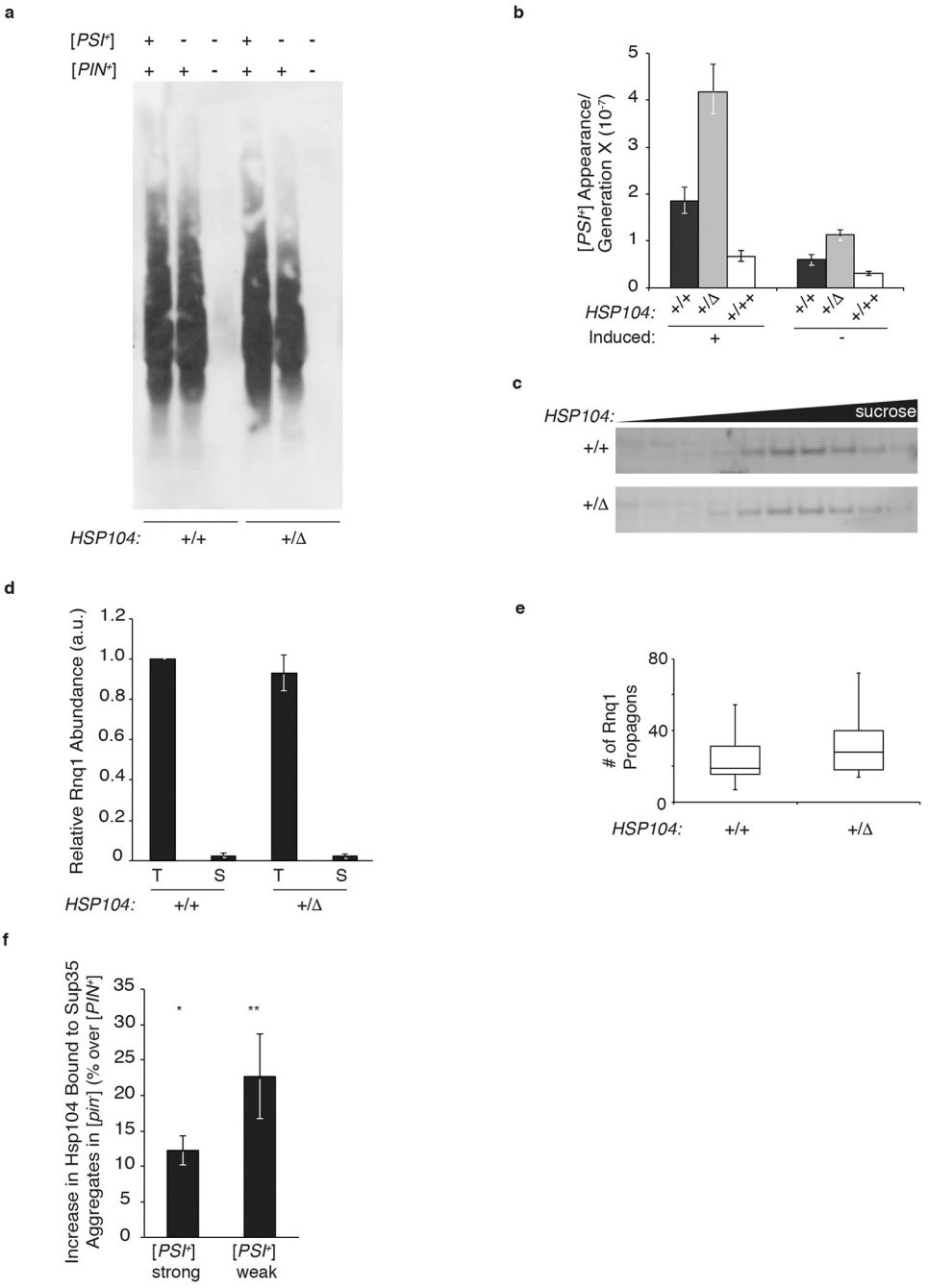

Fig 2.

Changes in Hsp104 levels and binding impact [*PSI*$^+$] appearance but not [*PIN*$^+$] propagation. **a.** Lysates from the indicated strains were analyzed by SDD-AGE and immunoblotting for Rnq1. Immunoblot shown is representative of three independent experiments performed with independent cultures. **b.** The frequencies of [*PSI*$^+$] appearance in diploid [*PIN*$^+$][*psi*$^-$] yeast strains with wildtype (+/+, black), heterozygous disruptions of *HSP104* (+/Δ. gray), or an extra copy of *HSP104* (+/++, white) were determined following transient overexpression of the Sup35 prion-determining domain (+) or in uninduced controls (−) by a fluctuation test. Data shown as means, error bars represent the 95% confidence interval from at least 8

independent cultures. **c.** Lysates from [*PIN*$^{+}$] strains with wildtype (+/+) or a heterozygous disruption of *HSP104* (+/Δ) were analyzed by sucrose gradient, SDS-PAGE and immunoblotting for Rnq1. Immunoblots are representative of three independent experiments performed with independent cultures. **d.** The fraction of total (T) and soluble (S) Rnq1 was determined in lysates from diploid yeast strains wildtype (+/+) or heterozygous disruptions of *HSP104* (+/Δ). Data are mean and s.d. from 3 independent experiments performed with independent cultures. **e.** The number of Rnq1 propagons was determined in the diploid yeast strains with wildtype (+/+) or a heterozygous disruption of *HSP104* (+/Δ). Horizontal lines on boxes indicate 25th, 50th, and 75th percentiles; error bars indicate 10th and 90th percentiles from at least 8 independent experiments performed with independent cultures. **f.** Binding of Hsp104 to Sup35 aggregates was determined in [*PIN*$^{+}$] or [*pin*$^{-}$] yeast strains propagating [*PSI*$^{+}$]^{Strong} or [*PSI*$^{+}$]^{Weak} by immunocapture of HA-NM. The increase in Hsp104 binding to Sup35 aggregates in the [*pin*$^{-}$] strains is expressed as a percentage over the binding level observed in the [*PIN*$^{+}$] strains. Data are means and s.d. from 3 independent experiments performed with independent cultures. *p = 0.005; **p = 0.002 by two-tailed Student's t-test. Data for graphs in panels b and d-f and uncropped images for panel c are available as source data.

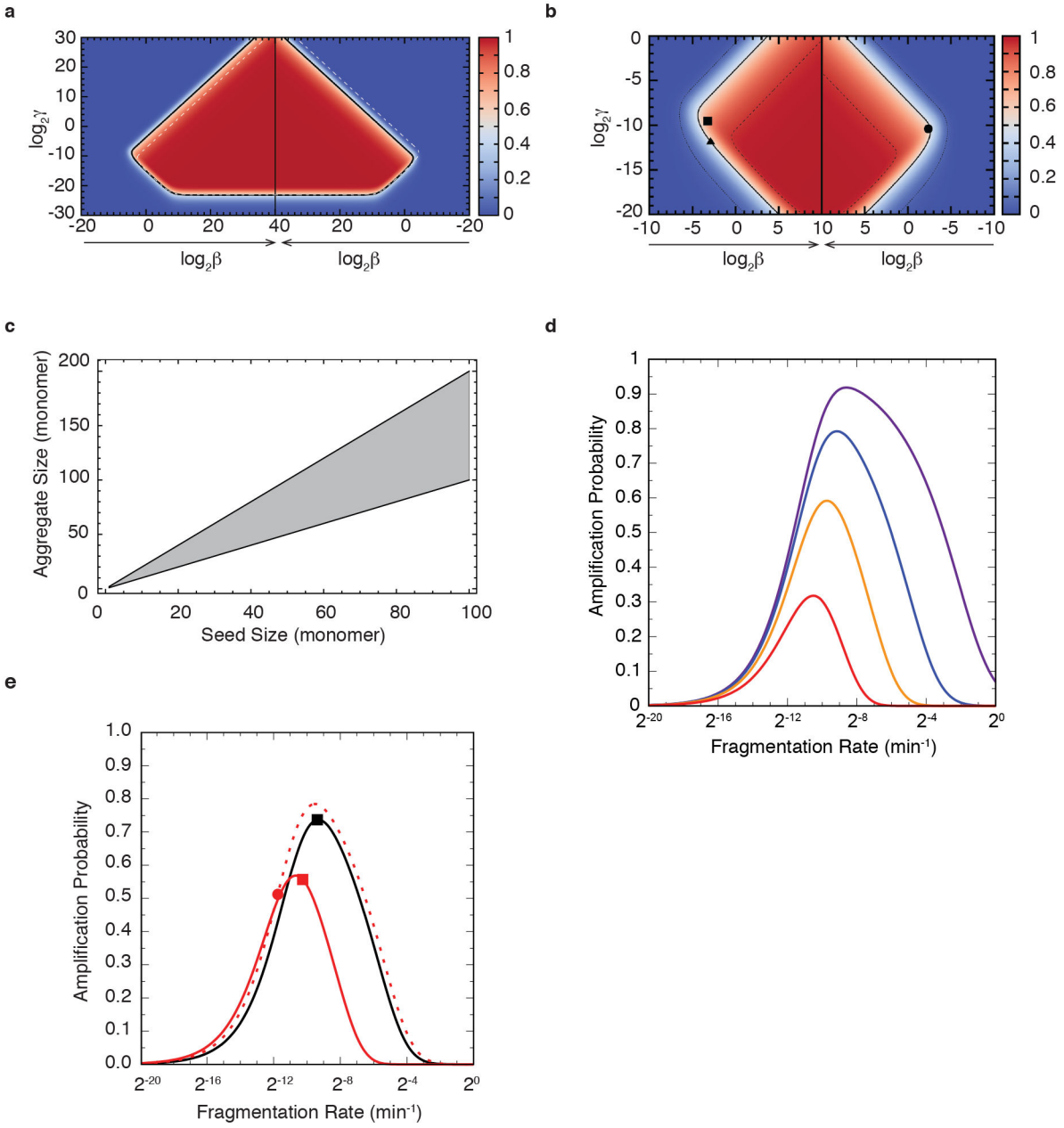

Fig. 3.

Mathematical modeling reveals the impact of seed size on [*PSI*$^{+}$] stability. **a.** A heat map from a stochastic persistence model of Sup35 aggregate dynamics *in vivo* indicates the probabilities of loss (blue) of a single Sup35 aggregate as a function of conversion (β) and fragmentation (γ) rates with a seed size of five (left) or fifteen (right). The black solid line indicates 50% loss; the dashed white line indicates 50% loss on the opposite side of the heat map (i.e. for n_s=5 on the n_s=15 heat map). **b.** The heat map from panel (a) is expanded to focus on the positions of [*PSI*$^{+}$]$^{\text{Strong}}$ with a n_s of five (black square), [*PSI*$^{+}$]$^{\text{Weak}}$ with a n_s of five (black triangle), and [*PSI*$^{+}$]$^{\text{Weak}}$ with a n_s of fifteen (black circle). Dotted line indicates 95% loss; solid line indicates 50% loss, and dashed line indicates 5% loss. **c.** Diagram of the

sensitivity of aggregates based on their size (gray) to a single fragmentation event as a function of seed size. **d.** The stochastic persistence model determines the probability of amplification of a single Sup35 aggregate as a function of fragmentation rate with seed sizes of 2 (purple), 4 (blue), 8 (orange), and 16 (red). **e.** A comparison of the probability of amplification of a single aggregate for [*PSI*$^{+}$]$^{\text{Strong}}$ as a function of fragmentation rate with a seed size of five (black curve), [*PSI*$^{+}$]$^{\text{Weak}}$ with a seed size of five (red dotted curve), or [*PSI*$^{+}$]$^{\text{Weak}}$ with a seed size of fifteen (red solid curve). The exact positions of [*PSI*$^{+}$]$^{\text{Strong}}$ (black square), [*PSI*$^{+}$]$^{\text{Weak}}$ (red circle or square) are indicated on each curve.

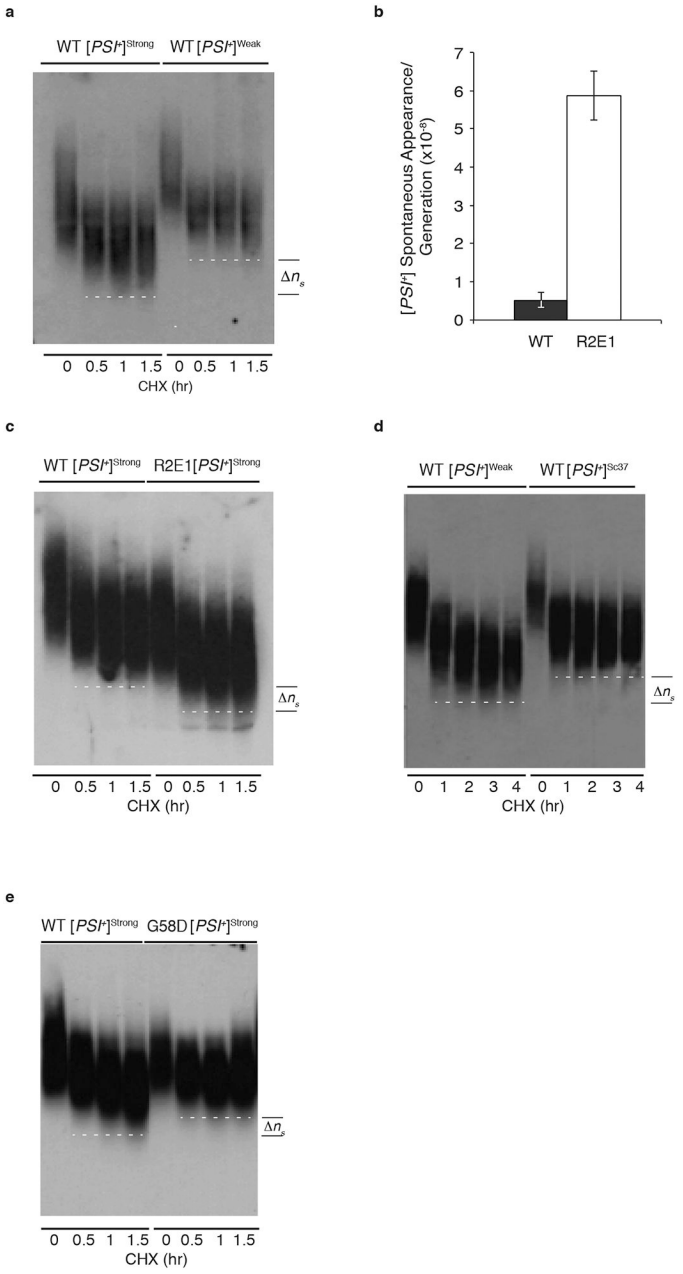

Fig. 4.

Differences in seed size explain previously unexplained aspects of [*PSI*$^+$] curing and appearance. **a.** Diploid yeast strains propagating the [*PSI*$^+$]^{Strong} or [*PSI*$^+$]^{Weak} variants were treated with cycloheximide (CHX) for the indicated times, and lysates were analyzed by SDD-AGE and immunoblotting for Sup35. The difference in the lower boundaries of the aggregate distributions following treatment with cycloheximide reveals differences in seed size between the two amyloids (Δn_s). **b.** The frequency of spontaneous [*PSI*$^+$] appearance in a [*PIN*$^+$][*psi*$^-$] yeast strain with wildtype Sup35 (WT) or the R2E1 mutant was determined by a fluctuation test. Data shown as means; error bars represent the 95% confidence interval from at least17 independent cultures. **c, d, e.** Diploid yeast strains expressing wildtype,

R2E1 or both WT and G58D Sup35 and the indicated [*PSI*$^{+}$] variant were treated with cycloheximide (CHX) for the indicated time, and lysates were analyzed by SDD-AGE and immunoblotting for Sup35. Differences in seed size between the two amyloids (Δn_s) are indicated, as detailed for panel a. The immunoblots shown in panels a,c,d,e are each representative of three independent experiments performed with independent cultures. Data for the graph in panel b are available as source data.

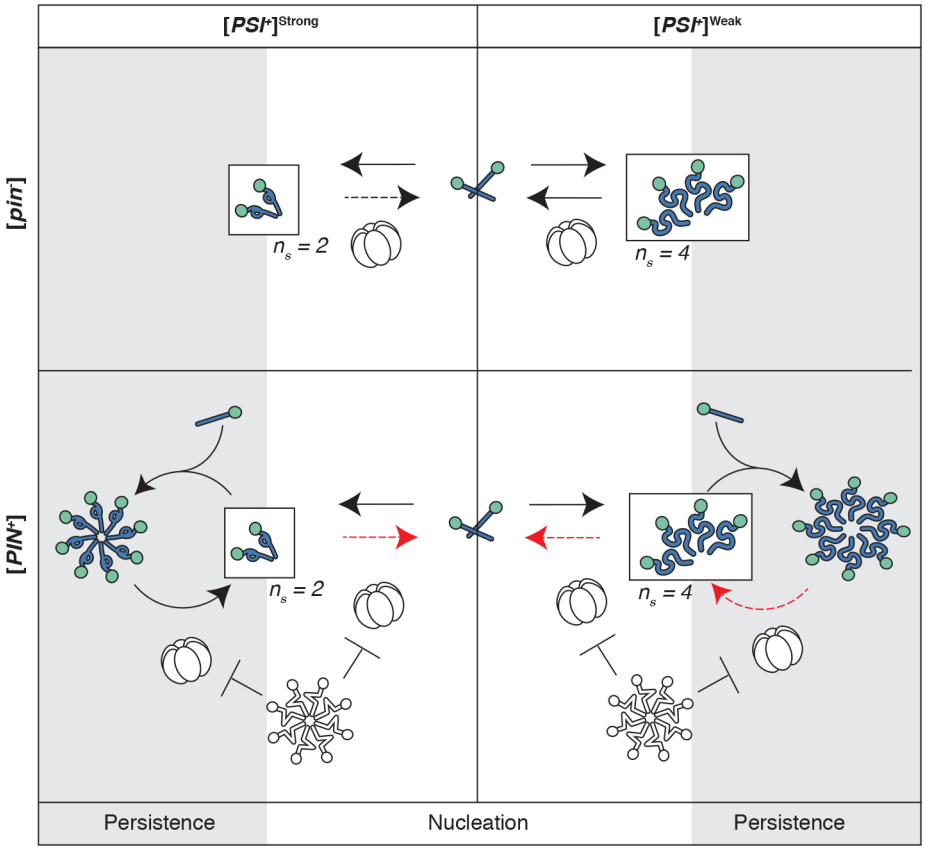

Fig. 5.

Schematic of biochemical processes impacting transitions between the [*PSI*$^+$] and [*psi*$^-$] states. Non-prion state Sup35 (ball and stick, middle) spontaneously adopts the [*PSI*$^+$]^{Strong} prion conformation (ball and corkscrew, left) or [*PSI*$^+$]^{Weak} prion conformation (ball and serpentine, right), which self-assemble into aggregates (top straight arrow) as a nucleation-dependent process. Seeds (boxed species) are smaller in size (n_s) for the [*PSI*$^+$]^{Strong} than the [*PSI*$^+$]^{Weak} conformation. In [*pin*$^-$] strains (top panels), the action of Hsp104 on seeds (bottom straight arrows) leads to their disassembly and the return of Sup35 to the non-prion state more efficiently for variants with larger seeds (i.e. solid straight arrow for [*PSI*$^+$]^{Weak} *vs.* dashed straight arrow for [*PSI*$^+$]^{Strong}). In [*PIN*$^+$] strains (bottom panels), aggregates of Rnq1 (unfilled pinwheel) are alternative substrates for Hsp104 and reduce its activity in several reactions (red arrows), which lead to observable changes in prion appearance and propagation. First, Sup35 seeds are fragmented less frequently (straight, dashed, red arrow) by Hsp104 (hexamer) in the presence of [*PIN*$^+$] to allow their persistence and the appearance of [*PSI*$^+$] through the templated conversion of non-prion state Sup35, which binds to and is incorporated into seeds (top curved arrows) to create larger aggregates (colored pinwheels). Second, the Hsp104-dependent fragmentation (bottom curved arrows) of these larger aggregates for the [*PSI*$^+$]^{Weak} variant, which is normally inefficient, is further reduced (curved, dashed, red arrow) in the presence of [*PIN*$^+$], interfering with the propagation of this variant.